Simultaneous subset tracing and miRNA profiling of tumor-derived exosomes via dual-surface-protein orthogonal barcoding

Yanmei Lei
Shanghai Jiao Tong University
Xiaochen Fei
Shanghai Jiao Tong University School of Medicine
Yue Ding
Shanghai Jiao Tong University School of Medicine
Guihua Zhang
Shanghai Jiao Tong University School of Medicine
Jia Song
Shanghai Jiao Tong University
Ying Zhuo
Southwest University
Wei Xue
Shanghai Jiao Tong University School of Medicine
Peng Zhang
Renji Hospital, Shanghai Jiao Tong University School of Medicine
Chaoyong Yang (cyyang@xmu.edu.cn)
Xiamen University https://orcid.org/0000-0002-2374-5342

Article

Keywords:

Posted Date: February 2nd, 2023

DOI: https://doi.org/10.21203/rs.3.rs-2404819/v1

Additional Declarations: There is **NO** Competing Interest.

Simultaneous subset tracing and miRNA profiling of tumor-derived exosomes via dual-surface-protein orthogonal barcoding

Yanmei Lei[1*], Xiaochen Fei[1*], Yue Ding[1], Guihua Zhang[1], Jia Song[1], Ying Zhuo[3✉], Wei Xue[1✉], Peng Zhang[1✉], Chaoyong Yang[1,2✉]

[1] Institute of Molecular Medicine, Department of Urology, Renji Hospital, School of Medicine, Shanghai Jiao Tong University, Shanghai 200127, China.

[2] The MOE Key Laboratory of Spectrochemical Analysis and Instrumentation, Key Laboratory for Chemical Biology of Fujian Province, State Key Laboratory of Physical Chemistry of Solid Surfaces, Department of Chemical Biology, College of Chemistry and Chemical Engineering, Xiamen University, Xiamen 361005, China.

[3] Key Laboratory of Luminescence Analysis and Molecular Sensing (Southwest University), Ministry of Education, College of Chemistry and Chemical Engineering, Southwest University, Chongqing 400715, China.

[*]These authors contributed equally to this work.

[✉]email: yingzhuo@swu.edu.cn; xuewei@renji.com; pengzhang016@sjtu.edu.cn; cyyang@xmu.edu.cn

Abstract

MicroRNAs (miRNAs) have been extensively studied as non-invasive biomarkers for cancer diagnosis and prognosis, while the clinical application was constrained by the heterogeneous miRNA sources in plasma and the tedious assay processes. Here we developed a one-pot assay called dual-Surface-protein-guided Orthogonal Recognition of Tumor-derived Exosomes and in-situ profiling of microRNAs (SORTER) for rapid and precise diagnosis of prostate cancer. The SORTER utilizes the orthogonal barcoding of two allosteric aptamers against exosomal marker CD63 and tumor marker EpCAM to recognize and sort tumor-derived exosome subtypes. Furthermore, the labeled barcode on tumor-derived exosomes guided the targeted fusion with liposome miRNA detection probes, enabling in-situ profiling of tumor-derived exosomal miRNAs. With a signature of six miRNAs, SORTER differentiated prostate cancer and benign prostatic hyperplasia with a sensitivity, specificity, and accuracy of 100% in the training and validation cohorts. The SORTER provides a promising tool to advance the clinical adaptability of miRNA-based liquid biopsy.

Introduction

MicroRNAs (miRNAs) are a class of short non-coding single-stranded RNAs (approximately 22 nucleotides) that play fundamental roles in gene expression regulation by repressing the translation of target genes or degrading their target transcripts[1, 2]. Dysregulated miRNAs are closely associated with the pathogenesis of a variety of cancers and thus have been studied as emerging biomarkers in cancer diagnosis, prognosis, and treatment monitoring[3, 4]. However, the clinical value of miRNAs in liquid biopsy was questioned by researchers, attributed to the heterogenous origins and existing forms of miRNAs in bodily fluids, such as circulating free miRNAs, miRNAs bounded with ribonucleoproteins, or encapsulated in different extracellular vesicles[5, 6]. The non-specific source of biomarkers diminishes the accuracy of miRNAs as a diagnostic tool and has become the stumbling block to moving from proof-of-concept to clinical application. Exosomes are a unique subtype of extracellular vesicles generated via endosomes and multivesicular bodies pathway[7, 8]. miRNAs are selectively packed and enriched in exosomes as regulators of a wide range of physiologic and pathologic processes, and keep stable under the protection of lipid membranes[9, 10]. In particular, tumor-derived exosomal miRNAs are closely associated with cancer progression[11] and afford great promise to enhance the specificity and accuracy of miRNA-based liquid biopsy. Unfortunately, the specific recognition of tumor-derived exosomes and quantitative detection of exosomal miRNAs are still technically challenging due to the complex background interference[12-14], heterogenous EV subtypes[15, 16], and varied expression levels of different exosomal miRNAs[17, 18]. In addition, the existing miRNA assays require multiple manual steps and take a long assay time. Therefore, developing a sensitive, accurate, and simplified bioassay to quantify tumor-derived exosomal miRNAs in complicated biofluid samples is highly desirable to promote the development of clinically viable miRNA biomarkers of cancer.

The prevailing RNA quantification technologies, such as quantitative reverse transcription-polymerase chain reaction (qRT-PCR) and next-generation sequencing (NGS), enable the detection of specific miRNA species in exosomes with high sensitivity down to fM[18, 19]. However, these technologies necessitate a large sample volume (> 500 μL) to obtain sufficient exosomes for RNA analysis and involve exosome concentration, RNA extraction, cDNA generation, and sequence amplification procedures[20, 21], which are laborious and time-consuming. Moreover, the analysis is susceptible to interference of free miRNAs in

biofluids, whose abundance is several orders higher than exosomal miRNAs[22-24]. Alternative to the sequence amplification-based strategies, a series of in-situ exosomal miRNAs bioassays have been recently developed by directly or indirectly importing DNA probes into membrane vesicles, such as gold nanoflares (Au NFs) and molecular beacons (MBs)[25-27]. Zhou et al. designed a virus-mimicking fusogenic vesicle-encapsulated MBs probe, which can rapidly detect extracellular vesicle miRNAs within 2 h via membrane fusion[28]. Zhao et al. proposed a thermophoretic sensor for in-situ extracellular vesicle miRNAs analysis by transporting Au NFs into vesicles, showing detection sensitivity down to 0.36 fM in 0.5 μL plasma samples[29]. These in-situ technologies provided efficient and robust extracellular vesicle miRNA detection without resorting to tedious RNA extraction and eliminated the background interference of complex biofluid samples. However, the transportation of miRNA probes into vesicles is stochastic and cannot distinguish tumor-derived exosomes from other non-specific vesicles. The ensemble detection of total EV miRNAs conceals the specificity of tumor-derived exosomal miRNA and reduces the accuracy in liquid biopsy applications.

Tumor-derived exosomes only account for a small fraction of EVs, thus challenging to distinguish them from other EVs precisely[30]. Surface protein receptors are routinely used to identify the unique subtype of various extracellular vesicles[12, 31]. Typically, the tetraspanin CD63 is often enriched in exosomes compared with other vesicles[32], and epithelial cell adhesion molecule (EpCAM) is a typical marker of tumor[33]. The orthogonal combination of the two proteins sets a more critical threshold and holds great promise in recognizing and sorting tumor-derived exosomes. A multi-receptor-based DNA logic device has recently been reported to bindle multiple aptamers into a single computing device and recognizes subpopulations of cells and exosomes[34-36]. For instance, Chuang et al. developed an AND Boolean logical device using multiple aptamers and toehold activation for signal integration and amplification to label and recognize target cell types via the synergistic presence of different surface protein receptors[37]. Our group reported that the dual-surface-protein-aptamer recognition combined with droplet digital PCR achieved the quantitative profiling of tumor-derived exosomal PD-L1[38]. However, to the best of our knowledge, this multiple protein receptors synergistic logic device has not been utilized in the selective recognition and sorting of exosome subtypes.

Addressing these challenges, here we developed dual-Surface-protein-guided Orthogonal Recognition of Tumor-derived Exosomes and in-situ probing of microRNA profiles (SORTER) for rapid and specific detection of tumor-derived exosomal miRNAs. The SORTER affords three significant advantages over the

existing exosomal miRNA biosensing assays. Firstly, the SORTER presents the first strategy to recognize and sort tumor-derived exosomes precisely, a small yet considerable subpopulation of extracellular vesicles, improving the diagnostic and prognostic accuracy of exosome-based liquid biopsy. Specifically, dual allosteric aptamers of exosome-specific marker CD63 and tumor marker EpCAM were employed to create a unique orthogonal identity barcode on tumor-derived exosomes, thus inducing the targeted recognition and controlled fusion of miRNA probes for signal amplification. Second, the in-situ miRNA detection inside the membrane structures of exosomes prevents the contamination of free circulation miRNAs and degradation of RNases from biofluid samples, enabling the accurate quantification and even dynamic monitoring of tumor-derived exosomal miRNAs. Third, we incorporate multiple processes into SORTER, such as exosome recognition, importing probes, miRNA signal transduction, and amplification, and create a separation- and washing-free tumor-derived exosomal miRNAs assay. The SORTER offers superior analytical performance towards liquid biopsy applications, which consumes only 0.2 μL plasma sample and completes the whole analysis in less than 2 h. We tested an exosome signature of six miRNAs (miR-222, miR-1290, miR-182, miR-21, miR-221, and miR-10b) in the training (n = 42) and validation (n = 32) cohorts, which can differentiate prostate cancer (PCa) and benign prostatic hyperplasia (BPH) with a sensitivity, specificity, and accuracy of 100%. The diagnostic accuracy also reached 90.6% in classification of metastatic and non-metastatic prostate cancer. We envisioned that the SORTER provides a promising tool to advance the analysis of tumor-derived exosomal miRNAs and promote the clinical adaptability of miRNA-based liquid biopsy.

Results

Working principle of SORTER.

The SORTER assay is designed to achieve specific recognition and sorting of tumor-derived exosome subtypes and in-situ sensitive probing of tumor-derived exosomal miRNA profiles, and further improve the miRNA-based diagnostic accuracy of prostate cancer. The whole workflow consists of six steps as shown in Fig.1, including sample collection, plasma preparation, barcode labeling of tumor-derived exosomes, targeted importation of miRNA detection probes, in-situ multiplexed miRNA profiling, and biostatistical analysis for cancer diagnosis. The streamlined processes are highly straightforward and thus enable the rapid and precise one-pot miRNA profiling in tumor-derived exosomes. The two significant innovations of

SORTER are: (i) selective labeling and sorting of tumor-derived exosomes through dual-surface-protein-guided orthogonal recognition, and (ii) in-situ sensitive quantification of miRNAs via duplex-specific nuclease (DSN) catalyzed signal amplification.

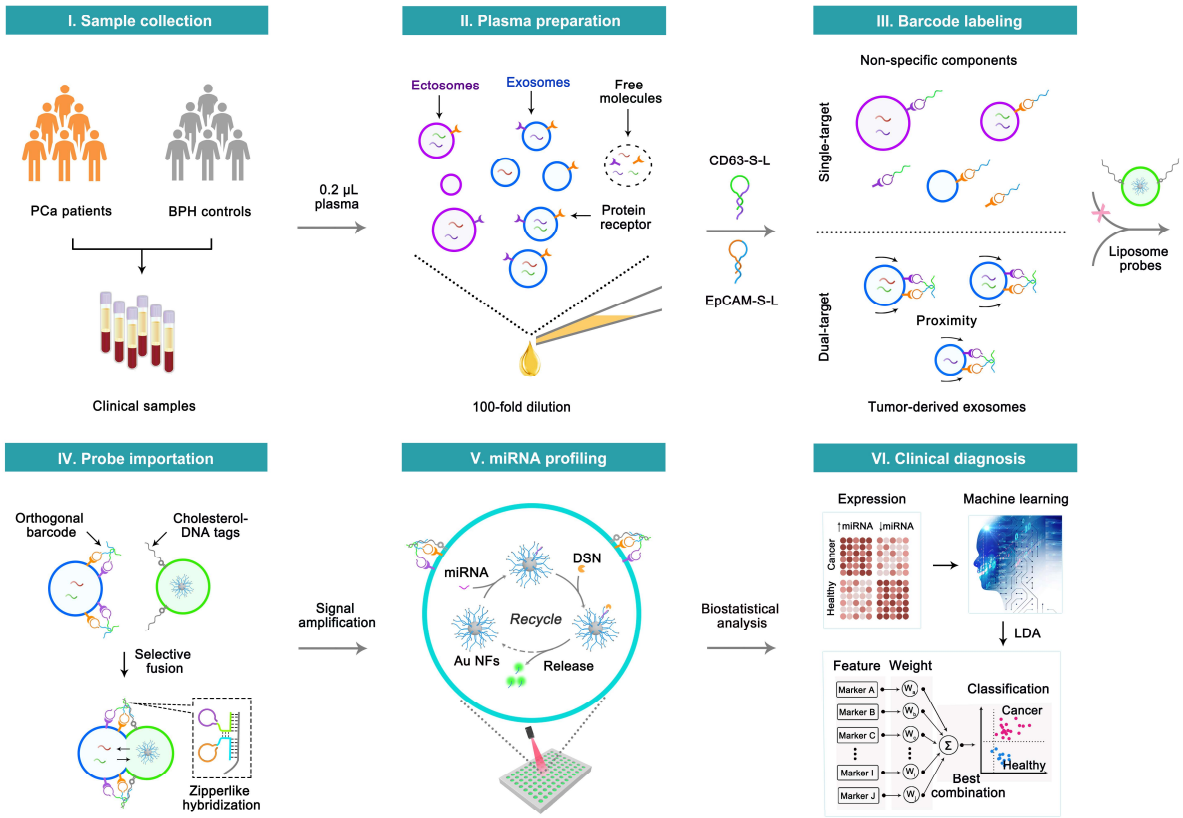

Fig. 1 Schematic illustration of SORTER assay for miRNA profiling of tumor-derived exosomes. I-II) Clinical plasma samples (0.2 μL) were collected from age-matched prostate cancer (PCa) patients and benign prostatic hyperplasia (BPH) controls. Exosomes, ectosomes, and free molecules produced by tumor and normal cells coexist in plasma samples and exhibit overlapping compositional features. **III**) Dual-surface-protein-guided orthogonal recognition barcode for the selective labeling of tumor-derived exosomes. The two allosteric aptamer probes (CD63-S-L and EpCAM-S-L) consist of three domains: the aptamer (CD63 or EpCAM) domain, the spacer (S) domain, and the linker (L) domain. The allosteric aptamer probes are in a non-active state with a hairpin structure, where the L domains are blocked for the subsequent reaction. When two protein receptors, CD63 and EpCAM, are recognized synergistically on a single exosome, two distinct L domains are exposed by allosteric transformation, creating a unique orthogonal barcode on tumor-derived exosomes via proximity-induced self-assembly. **IV**) The importation of miRNA detection probes into tumor-derived exosomes. The labeled barcode hybridized with complementary DNA tags anchored on liposome probes in a zipper-like behavior, bringing the bilayers into contact and facilitating membrane fusion to import miRNA detection reagents. **V**) Multiparametric assessment of miRNA profiles in tumor-derived exosomes. The SORTER incorporates multiple processes, including exosome recognition, importing probes, signal transduction, and amplification, permitting a sensitive and robust one-pot tumor-derived exosomal miRNAs assay. **VI**) The data processing and bioinformatic analysis for cancer diagnosis. The linear discriminant analysis (LDA) algorithm is used to identify the best combinations of miRNAs to classify PCa patients from BPH controls, and the LDA model then evaluates the predicted results.

There is no specific single marker to distinguish the heterogeneous sources of miRNAs in plasma selectively. In plasma samples, for example, tumor- and normal-derived exosomes, ectosomes, and free molecules (e.g., RNA-protein complexes) coexist and have overlapping compositional properties. Therefore, we leverage the combination of two typical surface protein markers, CD63 for exosomal-specific markers and EpCAM for the tumor-specific marker, to set up an orthogonal screening threshold and recognize tumor-derived exosomes from complicated biofluid samples precisely. Aptamers are promising tools for protein labeling because of their excellent specificity and affinity, low production costs, and configurational programmability[39-41]. We designed two allosteric aptamer probes of CD63 and EpCAM (detailed in Supplementary Fig. S1) as input units for orthogonal labeling of the tumor-derived exosome in clinical samples. The synergetic recognition of CD63 and EpCAM on a single exosome will trigger the allosteric transformation of aptamer probes, thus creating a unique orthogonal identity barcode on the tumor-derived exosome's surface via proximity-induced self-assembly. In particular, the unbounded aptamer probes are still in a non-active state, thus there is no need to wash away excess probes. The dual-target-protein-guided orthogonal barcoding method permits the rapid and selective labeling of tumor-derived exosomes in clinical samples, avoiding lengthy pre-isolation/purification processes and minimizing the non-specific interference of contaminated vesicles.

The quantification of tumor-derived exosomal miRNAs faces two major challenges: (i) the amount of circulating free miRNAs in the blood is several orders of magnitude more than target miRNAs in tumor-derived exosomes and cause serious interference to detection[15, 16, 42]; (ii) the concentration of miRNAs in tumor-derived exosomes is extremely low (approximately 1 copy/10^6 EVs to 1 copy/1 EV)[22-24], thus a superior sensitive assay is required for miRNA profiling. To address these issues, we designed a smart liposome probe (Tags-Lipo@Au NFs) to import miRNA detection probes into tumor-derived exosomes via targeted vesicle fusion and achieve in-situ sensitive quantification of various miRNAs inside exosomes. We utilized the orthogonal barcode on tumor-derived exosomes (Orth-Exo) to hybridize with complementary DNA tags anchored on liposome probes (Tags-Lipo@Au NFs), facilitating the selective recognition of tumor-derived exosomes and the simultaneous importation of miRNA detection probes. After that, the fluorescent signal of miRNAs was then generated and amplified using gold nanoflares (Au NFs) and duplex-specific nuclease (DSN) encapsulated in liposome probes. Specifically, the Au NFs were prepared by

immobilizing recognition sequences (5'-labeled-SH and 3'-labeled-FAM) onto spherical Au nanoparticles, where the fluorescence is effectively quenched by the Au surface, significantly minimizing the background signal. The target miRNA will bind with the DNA probe in the nanoflares to form DNA-RNA heteroduplexes. Notably, the DNA sequence in DNA-RNA heteroduplexes will be cleaved specifically by DSN to release fluorophore for fluorescence and RNA sequence, and initiate the target recycling and signal amplification process. The in-situ miRNA assay inside the membrane structures of exosomes eliminates the interference of circulating free miRNAs, and the Tags-Lipo@Au NFs probes provide the minimized background and amplified fluorescent signal, thus enabling highly selective and sensitive quantification of target miRNAs in tumor-derived exosomes.

Dual-surface-protein orthogonal barcode labeling on tumor-derived exosomes.

We selected a panel of nine membrane protein markers as candidates to distinguish the tumor and normal cell-derived exosomes: one exosome protein marker (CD63) and eight tumor protein markers, including EpCAM, nucleolin (NCL), carcinoembryonic antigen (CEA), human epidermal growth factor receptor 2 (HER2), mucin 1 (MUC1), programmed cell death 1 ligand 1 (PD-L1), prostate-specific membrane antigen (PSMA) and protein tyrosine kinase 7 (PTK7). Prostate cancer cell (LNCaP, PC-3) and benign prostatic hyperplasia cell (BPH-1)-derived exosomes (Exo) were used as the models of tumor-derived and normal-derived exosomes. The corresponding FAM-labeled aptamer probes (Supplementary Table S1) bind with the target proteins on the exosomes (Supplementary Fig. S2a), respectively. Flow cytometry analysis of LNCaP Exo and PC-3 Exo (Supplementary Fig. S2b-c) presents the highest expression level of EpCAM compared to the other seven tumor markers and indicates the best performance to distinguish tumor-derived exosomes (LNCaP, PC-3) from normal-derived exosomes (BPH-1). Therefore, the synergistic identification of target proteins CD63 (exosome marker) and EpCAM (tumor marker) is the best choice for recognizing and sorting tumor-derived exosomes.

To rapidly and selectively label tumor-derived exosomes with a traceable barcode in complex clinical scenarios, we design two allosteric aptamer probes of CD63 and EpCAM proteins as input units for orthogonal labeling of the tumor-derived exosome. The allosteric aptamer probes (CD63-S-L or EpCAM-S-L) consist of three domains: the aptamer (CD63 or EpCAM) domain, the spacer (S) domain, and the linker (L) domain. The allosteric aptamer probes are in their non-active configuration with a hairpin structure, and

188 the L domain is annealed and blocked for the downstream reaction. The aptamer domain of allosteric probes
189 can specifically recognize the target proteins, exposing the L domain by allosteric transformation. To confirm
190 whether CD63-S-L and EpCAM-S-L bind to target proteins and expose the L domain, we performed
191 fluorescence kinetic analysis on LNCaP Exo using fluorescence resonance energy transfer (FRET) couple
192 (BHQ1 and FAM) double-labeled CD63-S-L and EpCAM-S-L (Supplementary Fig. S3a-b). This allowed us
193 to easily monitor the allosteric transformation reaction through an increase in the fluorescence signal. When
194 the two allosteric aptamer probes of CD63-S-L or EpCAM-S-L were incubated with LNCaP Exo, the
195 fluorescence signal increased significantly, while almost no signal changes were observed in the control
196 experiments (CD63-S-L or EpCAM-S-L only). These findings validated that the designed allosteric aptamer
197 probes of CD63-S-L or EpCAM-S-L can bind to target proteins of exosomes efficiently and trigger an
198 allosteric change to expose the L domain, allowing the orthogonal barcode labeling of tumor-derived
199 exosomes.

200 To confirm whether CD63 and EpCAM are co-expressed on a single tumor-derived exosome surface,
201 we utilized a total internal reflection fluorescent microscope (TIRFM) to image CD63-S-L (3'-labeled-FAM)
202 and EpCAM-S-L (5'-labeled-Cy5) double-labeled tumor LNCaP Exo and normal BPH-1 Exo. Fig. 2a
203 illustrated CD63-S-L (FAM) and EpCAM-S-L (Cy5)-mediated orthogonal labeling on a single exosome
204 surface. Substantially strong fluorescent signals of CD63 (green dot) and EpCAM (red dot) were collocated
205 on the same particles of LNCaP Exo (orange dot in merged images), while very little colocation fluorescent
206 signals were detected from BPH-1 Exo (Fig. 2b). We further checked the labeling efficiencies of CD63-S-L
207 (FAM) and EpCAM-S-L (Cy5) on LNCaP Exo and BPH-1 Exo by flow cytometry (Fig. 2c). It was observed
208 that EpCAM-S-L (Cy5) has a substantially higher labeling efficiency on LNCaP Exo (10.6%) than BPH-1
209 Exo (0.73%), while CD63-S-L (FAM) has a better labeling efficiency on LNCaP Exo (1.23%) than BPH-1
210 Exo (0.23%). These findings show that CD63 and EpCAM proteins are expressed and coexist on a single
211 tumor-derived exosome surface and that CD63 and EpCAM probes can be effectively labeled on the same
212 vesicle surface.
213

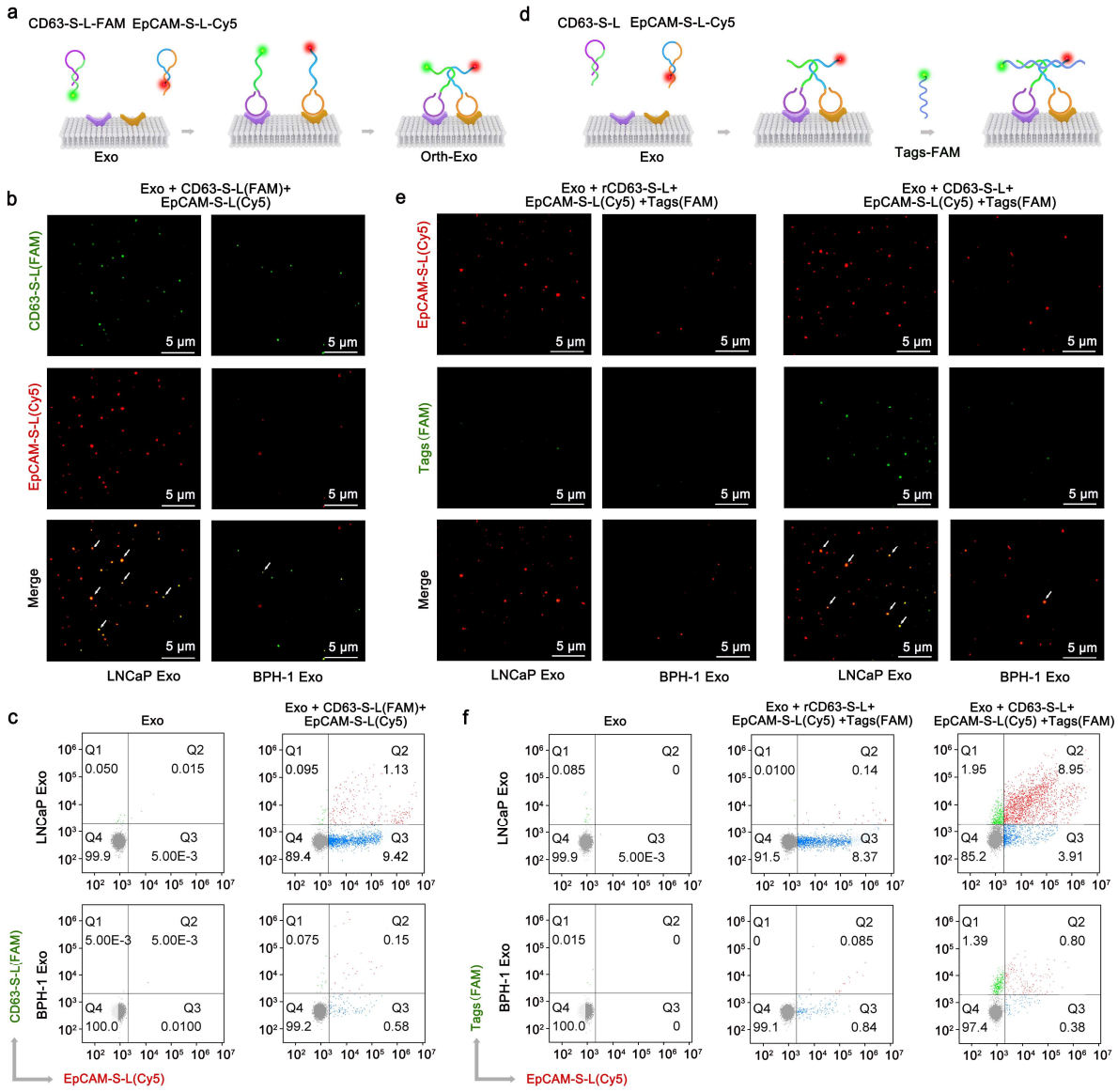

Fig. 2. Validation of dual-surface-protein orthogonal labeling on tumor-derived exosomes. a Schematics of CD63-S-L and EpCAM-S-L-mediated orthogonal labeling on a single exosome surface. **b-c** TIRFM images (**b**) and flow cytometry analysis (**c**) show the membrane proteins of CD63 and EpCAM expressed on LNCaP Exo and BPH-1 Exo. Blank group: Exo; Experimental group: Exo + CD63-S-L (3'-labeled-FAM) + EpCAM-S-L (5'-labeled-Cy5). **d** Schematics of the zipperlike hybridization of the orthogonal barcode-anchored exosome (Orth-Exo) and complementary DNA tags (Tags). **e-f** TIRFM images (**e**) and flow cytometry analysis (**f**) of the zipperlike hybridization of the orthogonal barcode and Tags against LNCaP Exo and BPH-1 Exo. Blank group: Exo; Control group: Exo + rCD63-S-L (only the aptamer domain is replaced by a random sequence) + EpCAM-S-L (5'-labeled-Cy5) + Tags (5'-labeled-FAM); Experimental group: Exo + CD63-S-L + EpCAM-S-L (5'-labeled-Cy5) + Tags (5'-labeled-FAM).

In order to validate the zipperlike hybridization of the orthogonal barcode-anchored exosome (Orth-Exo) and complementary DNA tags (Tags), we detected the CD63-S-L, EpCAM-S-L (5'-labeled-Cy5), and Tags (5'-labeled-FAM) co-labeled on LNCaP Exo and BPH-1 Exo and analyzed them by TIRFM. Fig. 2d

illustrated the zipperlike hybridization of the orthogonal barcode and Tags on a single exosome surface. As shown in Fig. 2e, the colocation of EpCAM-S-L (red dot) and Tags (green dot) on the same vesicle was evident in a part of the LNCaP Exo (orange dot in merged images) as compared to BPH-1 Exo. Additionally, no colocation fluorescent signals were observed when CD63-S-L was substituted with rCD63-S-L (only the CD63 aptamer domain is replaced by a random sequence). We further checked the labeling efficiencies of CD63-S-L, EpCAM-S-L (Cy5), and Tags (FAM) on LNCaP Exo and BPH-1 Exo by flow cytometry (Fig. 2f). Tags (FAM) have a substantially higher labeling efficiency on LNCaP Exo (8.95%) than BPH-1 Exo (0.80%). When CD63-S-L was replaced with rCD63-S-L, no apparent labeling signals were detected in both LNCaP Exo (0.14%) or BPH-1 Exo (0.09%). These studies revealed the successful formation of orthogonal barcodes on a single tumor-derived exosome surface and the effective zipperlike hybridization of DNA Tags and orthogonal barcodes on the same vesicle surface. Meanwhile, as shown in Supplementary Fig. S4a-b, we further measured the labeling intensities on LNCaP Exo with the following fluorescence sequences: CD63-S-L (3'-labeled-FAM), EpCAM-S-L (5'-labeled-FAM), Tags (5', 3'-labeled-FAM), and rCD63-S-L (3'-labeled-FAM). Flow cytometry analysis demonstrated that the formed orthogonal barcodes improved the binding affinities of allosteric aptamer probes and the zipperlike hybridization of Tags and orthogonal barcodes could occur on tumor-derived exosomes surface. In addition, the structural stability of orthogonal barcodes on a single exosome surface was estimated using the melting temperatures (Supplementary Fig. S4c). The results demonstrated that the orthogonal barcode has excellent structural stability on the vesicle surface, allowing for the effective zipperlike hybridization of DNA Tags and orthogonal barcode.

Dynamic monitoring of dual-surface-protein-guided liposome probe fusion.

The hybridization reaction between DNA tags on liposomes and orthogonal barcodes on tumor-derived exosomes guided the targeted fusion of liposomes and exosomes. The morphology and size of liposomes and LNCaP Exo were first characterized by nanoparticle tracking analysis (NTA) and transmission electron microscopy (TEM). The liposomes and exosomes were typical sphere- or cup-shaped vesicles and had a diameter of about 143 nm and 169 nm, respectively (Supplementary Fig. S5a-b). To confirm dual-surface-protein-guided liposome probe fusion, we monitored fusion-based membrane mixing using a FRET-based assay (Fig. 3a). DNA tags-anchored liposomes (Tags-Lipo) were double-labeled with the donor of 3,3'-dioctadecyloxacarbocyanine perchlorate (DiO, 501 nm) and the acceptor of 1,1'-dioctadecyl-3,3,3',3'

tetramethylindocarbocyanine perchlorate (DiI, 565 nm). After fusion, the membrane was enlarged, leading to decreased FRET efficiency between the DiO and DiI on the membrane surface. As presented in Fig. 3b, the FRET efficiency declined as the molar ratio of Tags-Lipo-DiO-DiI to orthogonal barcode-anchored exosomes (Orth-Exo) further increased. However, nearly no fusion was seen in the stochastic fusion between Lipo-DiO-DiI and exosome with no barcodes (Exo). The membrane fusion dynamic was also monitored in the FRET assay. When non-fluorescent Orth-Exo was incubated with double-labeled Tags-Lipo (Tags-Lipo-DiI-DiO), the DiO signals increased quickly and reached a plateau value in 2 h (Fig. 3c), while no change was seen in the stochastic fusion of Lipo-DiO-DiI and Exo. These results confirmed that the successful fusion is indeed mediated by the zipperlike hybridization between Orth-Exo and Tags-Lipo-DiI-DiO. Furthermore, the fusion mixing analyses of Tags-Lipo-DiO-DiI and Orth-Exo at different temperatures were recorded in Fig. 3d. With the increase in temperature, the stochastic fusion of Lipo-DiO-DiI and Exo also enhanced. Consequently, 37 °C was the optimum temperature for the SORTER assay holding maximized target to stochastic fusion efficiency ratio.

To further validate the effective fusion of Tags-Lipo and Orth-Exo, we labeled the Tags-Lipo and Orth-Exo with DiI and DiO, respectively (Fig. 3e). The DiI fluorescence of Tags-Lipo (red dot) colocalized well with that of DiO in Orth-Exo (green dot). In contrast, almost no detectable colocalized fluorescence signals were observed in the stochastic fusion between Lipo-DiI and Exo-DiO. Notably, we observed multiple Orth-Exo (green dot) around large overlapping particles (yellow dot), indicating that the orthogonal fusion of Orth-Exo and Tags-Lipo-DiI-Dio are DNA-programmed cascade reactions. The hydrodynamic size distribution of the membrane fusion product was determined by the dynamic light scattering method (DLS) at different time intervals (Fig. 3f). The diameter of the fused vesicles gradually increased from 154.7 to 206.5 nm, while the diameter barely enhanced owing to the lack of the zipperlike hybridization of Tags and orthogonal barcode in control experiments. TEM analysis of these vesicles (Fig. 3g) revealed the individual liposome or exosomes, which is consistent with incomplete fusion. However, the hemifusion intermediate or fully fused state was observed in the Tags-Lipo@Au NFs and Orth-Exo fusion reaction. These results demonstrate the effective dual-surface-protein-mediated orthogonal fusion of Orth-Exo and Tags-Lipo, allowing for the importation of the encapsulated miRNA detection probes for downstream analysis.

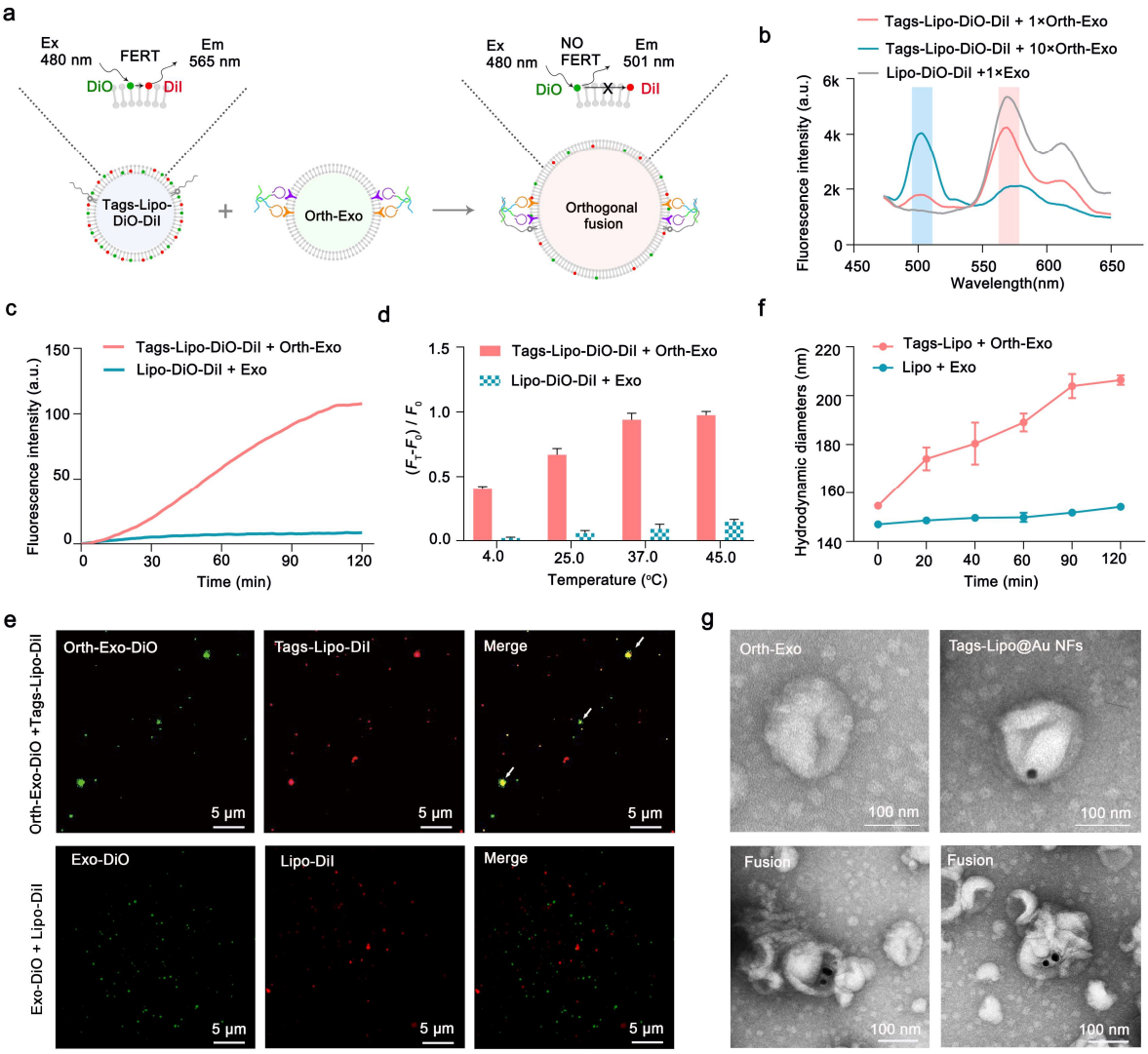

Fig. 3. Dynamic monitoring of dual-surface-protein-guided liposome probe fusion. a Schematic illustration of the FRET-based lipid membrane mixing for investigating the orthogonal fusion between Orth-Exo and Tags-Lipo-DiO-DiI. The fusion event was measured by the decreased FRET efficiency between the donor (DiO, 501 nm) and acceptor (DiI, 565 nm). **b** Fluorescence spectra analysis of the orthogonal fusion between Tags-Lipo-DiO-DiI and 1× and 10× molar ratios Orth-Exo. Negative control for the stochastic fusion of Lipo-DiO-DiI and Exo. **c** Fluorescence kinetic analysis of the target fusion between Tags-Lipo-DiO-DiI and Orth-Exo. Negative control for the stochastic fusion between Lipo-DiO-DiI and Exo. **d** Fusion mixing analysis of Tags-Lipo-DiO-DiI and Orth-Exo at different temperatures. Control experiment for the stochastic fusion between Lipo-DiO-DiI and Exo. The data represents mean ± s.d (n = 3). **e** TIRFM images showing the orthogonal fusion between the Tags-Lipo-DiI and Orth-Exo-DiO and the stochastic fusion between Lipo-DiI and Exo-DiO. **f** Diameters of the fusion products are determined by the DLS method at different time intervals. The data represents mean ± s.d (n = 3). **g** TEM images of Orth-Exo only, Tags-Lipo@Au NFs only, and the fusion vesicles of Tags-Lipo@Au NFs and Orth-Exo.

SORTER for tumor-derived exosomal miRNA analysis.

Prostate cancer (PCa) is one of the most prevalent diagnosed malignancies affecting men worldwide, with increasing cancer-related mortality [43-45]. Currently, the widely used serum prostate-specific antigen

(PSA) screening lacks sufficient specificity and sensitivity for clinical diagnosis of PCa. Patients with benign prostatic hyperplasia (BPH) frequently have elevated PSA levels, leading to needless prostate biopsy and overtreatment [46, 47]. Therefore, it is urgent to develop a liquid biopsy assay to facilitate the early diagnosis of PCa, which is crucial to improve long-term clinical outcomes. miRNAs inside tumor-derived exosomes, closely associated with PCa development, invasion, and metastasis[48, 49], are potential liquid biopsy biomarkers for PCa diagnosis. Here we developed the sensitive and robust one-pot SORTER assay to enable multiparametric miRNA profiling of tumor-derived exosomes in PCa plasma samples. Several putative PCa-associated miRNAs were thus selected to be detected in tumor-derived exosomes, including miR-21, miR-222, miR-1290, miR-221, miR-10b, and miR-182. The SORTER incorporates multiple processes (Fig. 4a), including exosome recognition, probe importation, fluorescent signal transduction, and amplification. To evaluate the assay performance of SORTER, we selected miR-21 as a model to optimize the experimental conditions. The optimum temperature for DSN activity was 37 °C, and the optimum amount of DSN enzyme was 1 U in a 300 μL reaction volume (Supplementary Fig. S6a-b). Furthermore, the sensitivity of the SORTER system was verified by incubating bare Au NFs with the synthesized miR-21. The detection limit of target miRNA is about 160 fM (Supplementary Fig. S7a-b), which performs similarly to the RT-PCR approach.

Under optimized assay conditions, we further evaluate the SORTER assay for tumor-derived exosomal miR-21 analysis. As shown in Fig. 4b, the fluorescent signal of LNCaP Exo increased significantly after incubation with Tags-Lipo@Au NFs ($P < 0.001$). In contrast, almost no signal change was observed in BPH-1 Exo after incubation with Tags-Lipo@Au NFs, or in BPH-1 Exo and LNCaP Exo after incubation with Lipo@Au NFs. Furthermore, flow cytometry and TIRFM results (Fig. 4c-d) further showed that tumor LNCaP Exo had significantly higher fluorescence than BPH-1 Exo. These results indicated an elevated level of miR-21 in the tumor exosomes. The sensitivity of the SORTER approach was determined by probing the miR-21 in purified LNCaP Exo spiked in both PBS and healthy plasma (Fig. 4e). Analysis of spiked plasma demonstrated comparable analytical merits to those of spiked PBS, such as calibration sensitivity (that is, the slope: 1.416 versus 1.412) and LOD (44.42 pg mL^{-1} versus 29.66 pg mL^{-1}). We next characterized the performance of SORTER by measuring the expression levels of six miRNAs in tumor-derived exosomes, including miR-21, miR-222, miR-1290, miR-221, miR-10b, and miR-182, in three PCa cells (PC-3, LNCaP,

and DU145) and one benign prostatic hyperplasia cell (BPH-1)-derived exosomes. As shown in Fig. 4f, experimental results showed that the expressions of these miRNAs in tumor-derived exosomes are significantly higher than in normal BPH-1 Exo (Fig. 4d). Such high sensitivity allowed us to detect a low level of exosomal miR-21 directly in PCa patient plasma, as verified by the measurements of a PBS blank and a control plasma (P<0.001; Fig. 4g). Additionally, all six miRNAs have significantly greater expression levels in PCa compared to BPH control plasma samples (Supplementary Fig. S8).

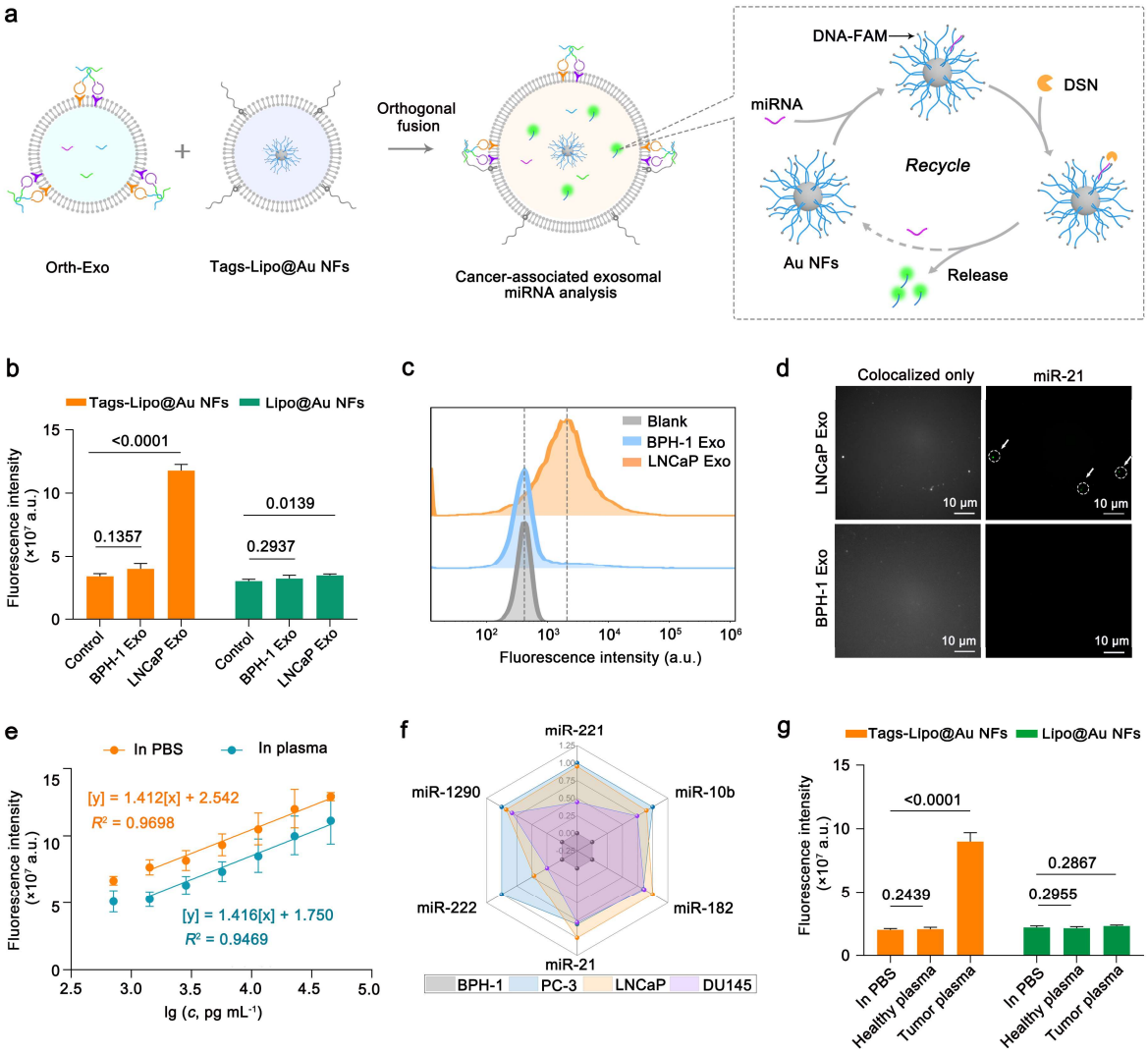

Fig. 4. SORTER for tumor-derived exosomal miRNA analysis. a Schematic illustration of the SORTER approach for tumor-derived exosomal miRNA analysis. **b-d** Fluorescence intensity (**b**), flow cytometry (**c**), TIRFM (**d**) analysis of miR-21 expression in orthogonal barcode-based BPH-1 Exo or LNCaP Exo (11.37 ng mL^{-1}) after incubation with Tags-Lipo@Au NFs and Lipo@Au NFs, respectively. The *P*-value was determined by a two-sided, parametric *t*-test. The data represents mean ± s.d ($n = 3$). **e** Calibration curves for quantifying LNCaP-derived exosomal miR-21 spiked in PBS and EV-depleted plasma (diluted by 100-folds in 1×PBS). Data represents mean ± s.d ($n = 3$). **f** The Radar plot shows six miRNA markers from the four cell

lines-derived exosomes (11.37 ng mL^{-1}), including three PCa cells (PC-3, LNCaP, and DU145) and one benign prostatic hyperplasia cell (BPH-1). **g** SORTER approach for miR-21 analysis in the fused vesicles after incubating with Tags-Lipo@Au NFs and Lipo@Au NFs in healthy and cancer plasma samples. The *P*-value was determined by a two-sided, parametric *t*-test. The data represents mean ± s.d ($n = 3$).

Clinical evaluation of SORTER for tumor-derived exosomal miRNA profiling.

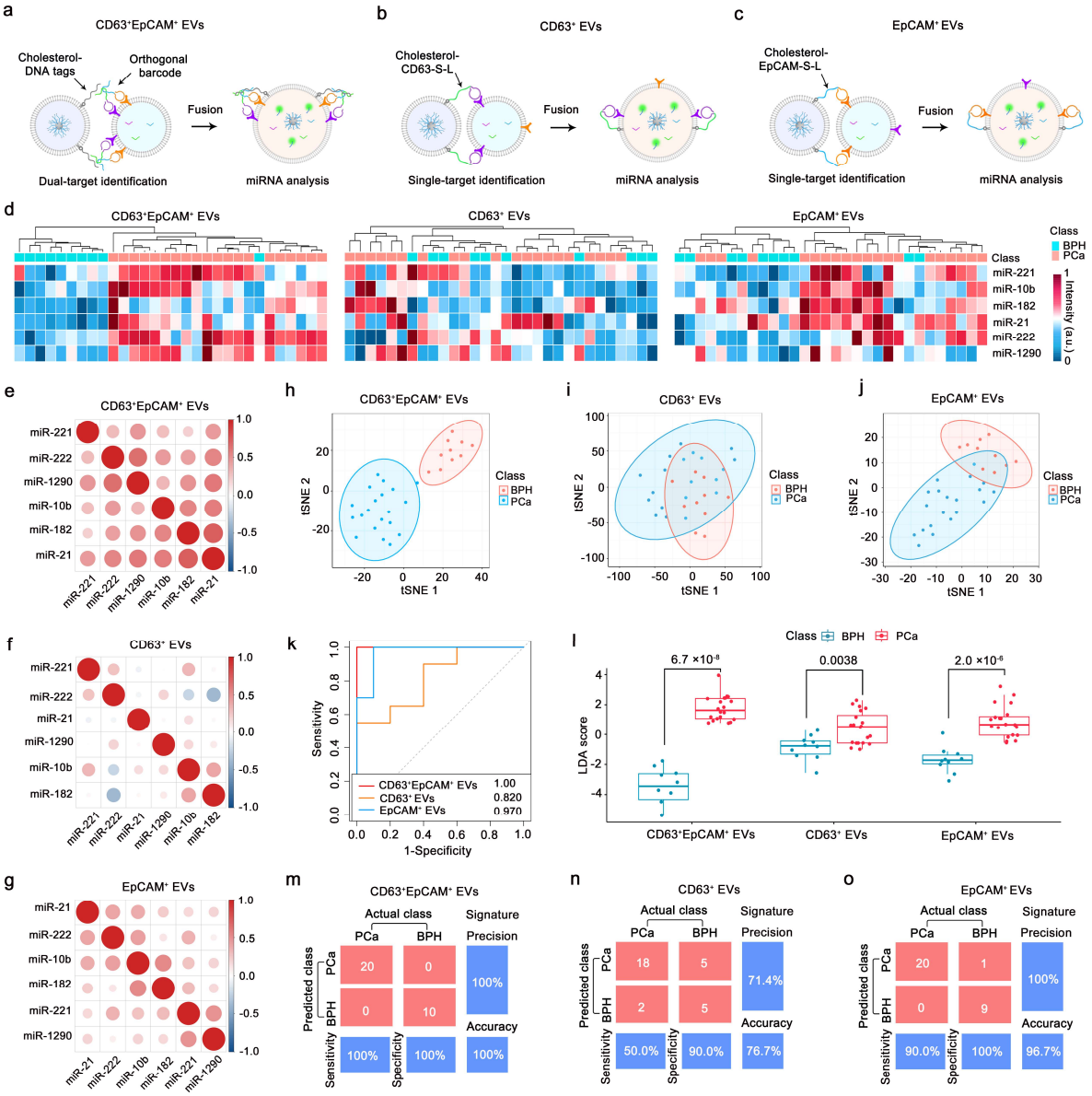

Fig. 5. Clinical evaluation of SORTER for tumor-derived exosomal miRNA profiling. **a-c** Schematic illustration of the miRNA analysis in the $CD63^+$ (**a**), $EpCAM^+$ (**b**), and $CD63^+EpCAM^+$ (**c**) EVs subpopulations. The identification of the $CD63^+$ or $EpCAM^+$ EVs subpopulation was performed by single-target recognition of CD63 or EpCAM protein on a single-particle membrane, and their miRNA analysis was achieved by guided fusion of Lipo@Au NFs and $CD63^+$ or $EpCAM^+$ EVs subpopulation. **d** Heatmap of unsupervised hierarchical clustering (Pearson correlation, average linkage) of six miRNAs expression levels in $CD63^+$, $EpCAM^+$, and $CD63^+EpCAM^+$ EVs for distinguishing PCa patients ($n = 20$) from BPH controls ($n = 10$). The signal intensities were averaged over triplicate measurements of each sample and normalized by min-max

normalization after the background subtraction. **e-g** Correlation matrix of the expression profiles for the six miRNAs in $CD63^+$ (**e**), $EpCAM^+$ (**f**), and $CD63^+EpCAM^+$ EVs (**g**). **h-j** t-distributed stochastic neighbor embedding (t-SNE) discriminated between PCa patients and BPH controls using the six markers as the input in $CD63^+$(**h**), $EpCAM^+$(**i**), and $CD63^+EpCAM^+$ EVs (**j**). **k** ROC curves for the PCa signature (weighted sum of six markers by LDA) in $CD63^+$, $EpCAM^+$, and $CD63^+EpCAM^+$ EVs to differentiate between PCa patients and BPH controls. **l** LDA score of the PCa signature in $CD63^+$, $EpCAM^+$, and $CD63^+EpCAM^+$ EVs for distinguishing PCa patients from BPH controls. The LDA score for the binary classification was generated using a linear combination of chosen markers weighted by the respective coefficients. The *P*-value was determined by a nonparametric, two-tailed Mann-Whitney *U* test. **m-o** Confusion matrix of the PCa signature in $CD63^+$(**m**), $EpCAM^+$(**n**), and $CD63^+EpCAM^+$ EVs (**o**). All statistical analyses were performed at 95% CIs.

To evaluate the clinical application performance of SORTER in the diagnosis of prostate cancer, we collected plasma samples from 30 patients (Supplementary Table S2) involving PCa (n = 20) and age-matched BPH (n = 10). We aimed to address (1) whether SORTER could recognize and analyze tumor-derived exosomes in plasma samples precisely and (2) whether SORTER could improve the diagnostic performance of exosome-based liquid biopsy. Using these samples (0.2 μL for each plasma sample), we performed multiparametric miRNA profiling using SORTER assay (termed $CD63^+EpCAM^+$ EVs in Fig 5a). As a comparison, the single-target (CD63 or EpCAM) guided fusion for miRNA profiling of $CD63^+$ or $EpCAM^+$ EVs was also conducted in the clinical cohort (Fig 5b-c).

By unsupervised hierarchical clustering analysis, we investigated whether a panel of six miRNAs for each patient exhibited mutually exclusive or similar expression patterns in different EV subpopulations (Fig 5d). The expression heatmap showed that the abundance of each miRNA has considerable heterogeneity for differentiating PCa and BPH in different EV subpopulations. The heterogeneous expression profile of miRNAs in the $CD63^+$, $EpCAM^+$, and $CD63^+EpCAM^+$ EVs subpopulations was separable into two different unsupervised classes. Six miRNAs (miR-222, miR-1290, miR-182, miR-21, miR-221, and miR-10b) were up-regulated in PCa compared to BPH plasma samples. These comparative analyses revealed the heterogeneity among overlapped EV subpopulations and corroborated the validity of the analytical data obtained by SORTER. Subsequently, pairwise comparisons of six miRNAs in different EV subpopulations were shown in Fig 5e-g. Six miRNAs do not correlate strongly with each other in these EV subpopulations, which drives us to the combinations of multiple markers for the accurate diagnosis of PCa. To explore the capacity of our method for PCa diagnosis, t-distributed stochastic neighbor embedding (t-SNE) is applied to discriminate between PCa and BPH (5h-j). Compared with $CD63^+$ and $EpCAM^+$ EVs, $CD63^+EpCAM^+$ EVs show a smaller overlap between the two patient groups. To further improve the diagnostic performance of

exosome-based liquid biopsy in differentiating PCa and BPH groups, we harnessed linear discriminant analysis (LDA) to compile all miRNA profiles. Using receiver operating characteristic (ROC) analyses, we determined sensitivity, specificity, and accuracy for each marker individually (Supplementary Fig. S9 and Supplementary Table S3) and also in PCa signature (weighted sum of six markers by LDA, Fig. 5k). We observed that no single marker achieved sufficiently high sensitivity and specificity. Notably, the multiparametric combination improved the performance of molecular phenotyping of exosomes for cancer diagnosis. The PCa signature in $CD63^+EpCAM^+$ EVs showed the best diagnostic performance with 100.0% [95% CI: 100-100%] area under the curve (AUC) compared with $CD63^+$ EVs [with 0.820 AUC (95% CI: 0.664-0.976)], and $EpCAM^+$ EVs [with 0.970 AUC (95% CI: 0.889-1.00)]. Furthermore, the assessment of our method for each marker individually and PCa signature in differentiating the BPH controls and PCa patients were shown in Fig. 5l and Supplementary Fig. S10). Compared with $CD63^+$ EVs (nonparametric, two-tailed Mann-Whitney *U* test, $P = 0.0038$) and $EpCAM^+$ EVs ($P = 2.0 \times 10^{-6}$), the LDA scores of PCa signature in $CD63^+EpCAM^+$ EVs ($P = 6.7 \times 10^{-8}$) were significantly different between the PCa and BPH groups. The classification results of marker combinations were further presented as confusion matrixes (Fig. 5m-o). The PCa signature in $CD63^+EpCAM^+$ EVs shows an extremely high sensitivity of 100%, specificity of 100%, and accuracy of 100% for distinguishing between PCa from BPH compared with $CD63^+$ EVs [with 50.0 sensitivity, 90.0% specificity, and 76.7% accuracy] and $EpCAM^+$ EVs [with 90.0% sensitivity, 100% specificity, and 96.7% accuracy]. These results demonstrated that our SORTER can improve the diagnostic detection performance of exosome-based liquid biopsy.

Clinical diagnosis of prostate cancer on SORTER.

To assess the diagnostic adaptability of the SORTER approach, we collected plasma from 74 patients participating in a clinical cohort (Supplementary Table S2), including non-metastatic PCa (nPCa, $n = 27$), metastatic PCa (mPCa, $n = 20$), and BPH ($n = 27$), of which 4/7 plasma samples were randomly assigned to the training cohort. Based on the SORTER approach to miRNA markers, the training cohort was studied first to generate the discriminant function model, which was then used to classify the patients in the validation cohort.

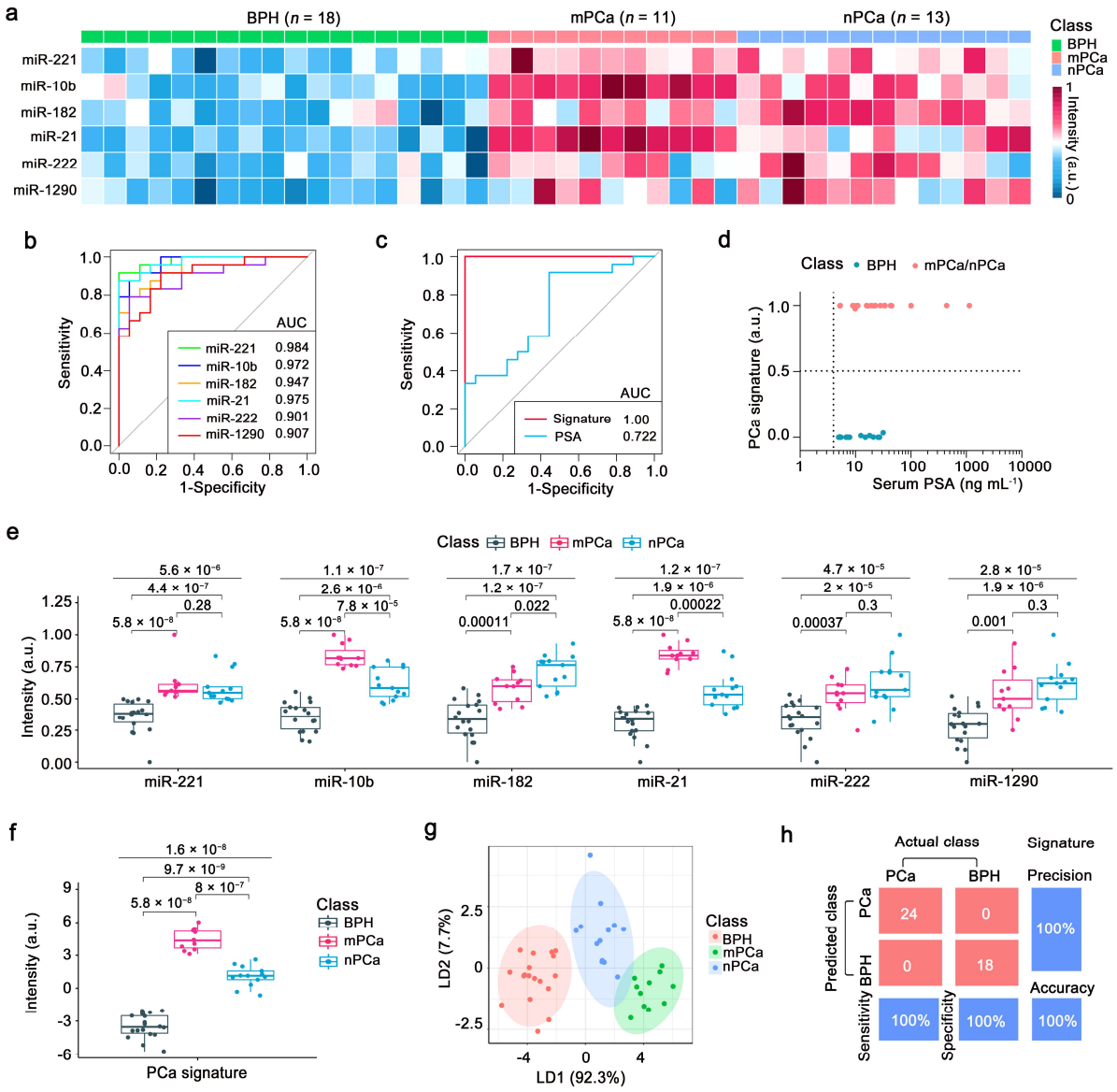

Fig. 6. SORTER for differentiation of nPCa, mPCa, and BPH in a training cohort. **a** Heatmap showing the abundance of the six miRNAs in a training set involving age-matched patients with BPH (n = 18), mPCa (n = 11), and nPCa (n = 13). The signal intensities were averaged over triplicate measurements of each sample and normalized by min-max normalization after the background subtraction. **b, c** ROC curves of the individual markers (**b**) and PCa signature (**c**) for PCa diagnosis. **d** Correlation of the PCa signature with serum PSA to differentiate nPCa/mPCa patients and BPH controls in a training cohort. The dashed line represents the threshold values for positivity (serum PSA, 4 ng mL^{-1}; PCa signature, 0.505). **e, f** Levels of the individual miRNA marker (**e**) and PCa signature (**f**) by SORTER approach at progressing disease stages. The overall and group pair P values were determined using Kruskal-Wallis one-way ANOVA with post hoc Dunn's test for pairwise multiple comparisons. **g** LDA plot using six miRNAs across nPCa, mPCa, and BPH patients. **h** Confusion matrix showed that the PCa signature had an accuracy of 100% across nPCa, mPCa, and BPH patients. All statistical analyses were performed at 95% CIs.

We first analyzed plasma from a training cohort of 13 nPCa, 11 mPCa, and 18 BPH patients. Fig. 6a summarized the abundance of six miRNAs for each subject in a training cohort. Each miRNA expression in

422 $CD63^+EpCAM^+$EVs has considerable heterogeneity for differentiating PCa and BPH groups. The diagnostic
423 metrics of individual markers or marker combinations were assessed using ROC curve analyses (Fig. 6b, c,
424 and Supplementary Table S4). For LDA-based ROC studies, the posterior probabilities from this binary
425 classification were employed as the sole test variable. Among six miRNA markers, no single marker achieved
426 sufficiently high sensitivity, specificity, and accuracy. The combination of the six markers comprising the
427 PCa signature [1.00 AUC, 100% sensitivity, 100% specificity, and 100% accuracy] afforded better diagnostic
428 ability than individual markers in the training cohort. We next correlated PCa signature analyses of
429 $CD63^+EpCAM^+$ EVs to serum PSA in PCa patients (Fig. 6d). The PCa signature was not correlated with PSA
430 in the training set ($r = 0.2084$; $P = 0.1854$). In the training cohort, 100% of BPH patients (18 of 18) showed
431 an increased concentration of PSA (>4 ng mL^{-1}, the threshold value used in the clinic cohort). In contrast,
432 only 0% of PCa patients (0 of 24) had a low PCa signature value (>0.505, the threshold value was obtained
433 using Youden's index based on the training cohort). Fig. 6e and 6f depict the assessment of our method for
434 detecting the BPH controls and two subgroups of nPCa and mPCa patients. We observed an overall
435 significant increase in PCa signature [Kruskal-Wallis one-way ANOVA analysis, $P = 1.6 \times 10^{-8}$] with
436 progressive disease stages when compared to individual markers. To further characterize the effectiveness
437 of our method to discriminate subgroups, we plotted the scores of each subject for the first two canonical
438 variables computed from the discriminant analysis (Fig. 6g). It was visualized that the training samples were
439 classified into three groups with notable separation among the patient groups at progressing disease stages.
440 The binary classification results of individual markers or marker combinations were further presented in
441 Supplementary Table S4 and Fig. 6h. The PCa signature shows an extremely high sensitivity of 100%,
442 specificity of 100%, and accuracy of 100% for distinguishing between PCa from BPH in the training cohort.
443 More importantly, all nPCa and mPCa cases in the training cohort were correctly detected, achieving an
444 overall accuracy of 100% (95% CI, 100.0 to 100.0%; Supplementary Fig. S11a).

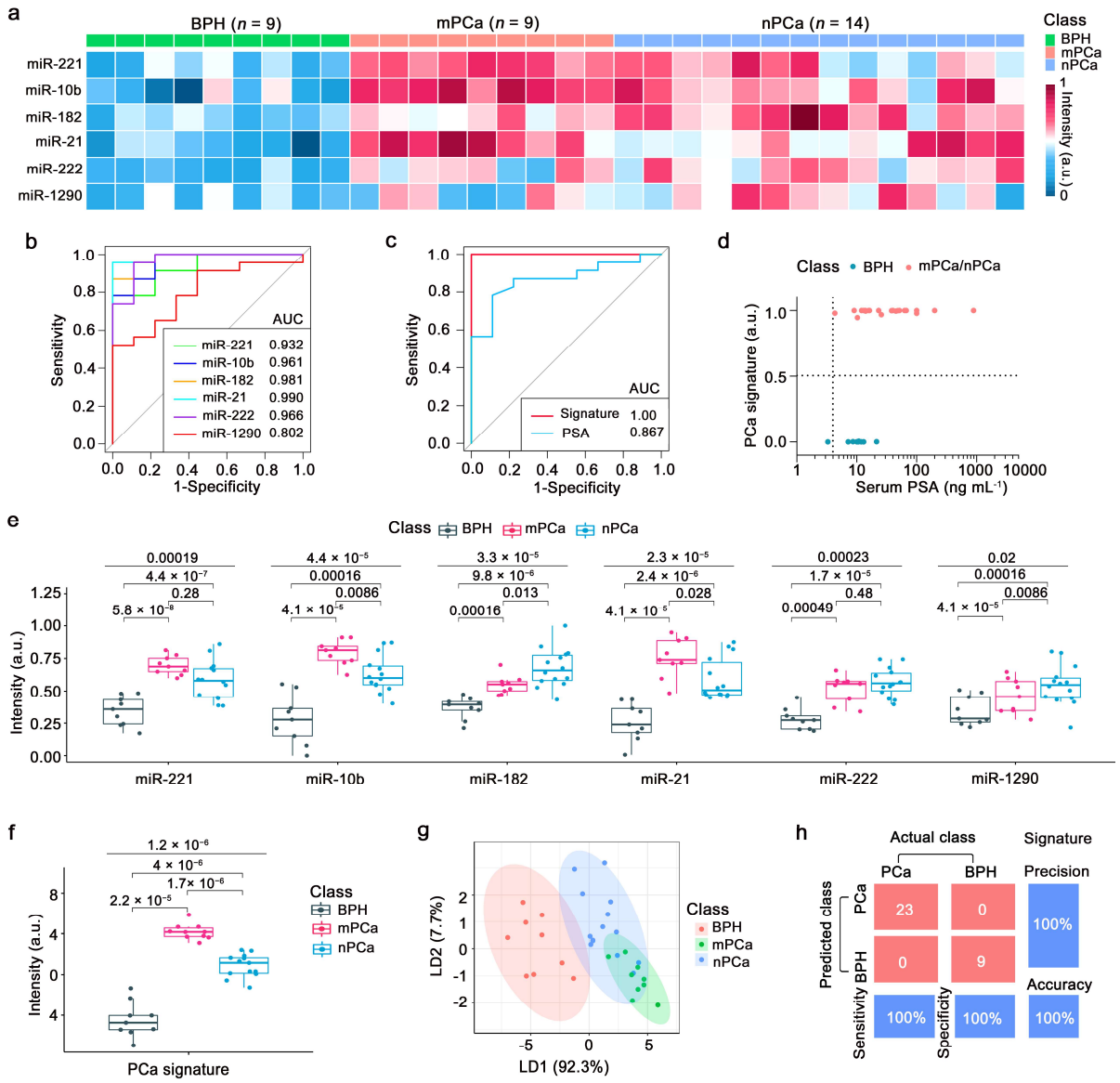

Fig. 7. Validation of the SORTER approach for PCa diagnosis. **a** Heatmap showing the abundance of the indicated miRNAs in a validation set involving age-matched patients with 14 nPCa, 9 mPCa, and 9 BPH. The data processing was similar to the training cohort (Fig. 6a). **b, c** ROC curves for the individual markers or marker combinations to differentiate between PCa patients and BPH controls in a validation cohort. **d** Correlation of the PCa signature with serum PSA to differentiate PCa and BPH. The threshold values were similar to those of the training cohort (Fig. 6d). **e, f** Levels of the individual miRNA marker (**e**), and PCa signature (**f**) by SORTER approach at progressing disease stages. The overall and group pair *P* values were calculated similarly to the training cohort (Fig. 6e, f). **g** LDA plot of the first two canonical variables derived from the discriminant analysis of the training cohort. **h** Confusion matrix showed that the PCa signature had an overall accuracy of 90.6% across nPCa, mPCa, and BPH patients. All statistical analyses were performed at 95% CIs.

The SORTER approach was further applied to an independent validation set of 32 age-matched plasma samples collected from 9 BPH controls, 14 nPCa, and 9 mPCa patients. Fig. 7a summarizes the performance of the indicated miRNAs for each patient. Analyzing the heatmap of each marker expression in

458 $CD63^+EpCAM^+$EVs once again showed a considerable heterogeneity for differentiating PCa and BPH. The
459 validation set data was then input into the trained LDA model to test its validity in cancer diagnosis. Across
460 the validation cohorts (Fig. 7b, c), the PCa signature [1.00 AUC, 100% sensitivity, 100% specificity, and
461 100% accuracy] once again showed excellent diagnostic performance for cancer diagnosis when compared
462 with a single marker. We also studied the correlation between PCa signature analyses and serum PSA in
463 patients with PCa and BPH (Fig. 7d). The PCa signature (r = 0.2018; P = 0.2681) was not correlated with
464 PSA. In the validation cohort, 88.9% of BPH patients (8 of 9) showed an increased concentration of PSA
465 (>4 ng mL^{-1}), whereas only 0% of PCa patients (0 of 13) had a low PCa signature value (>0.505). The
466 validation cohort data were then examined for identification of the PCa progressive stages using various
467 statistical methods. With the Kruskal-Wallis one-way ANOVA and post hoc Dunn's multiple comparisons
468 test (Fig. 7e, f), it was shown that the PCa signature ($P = 1.2 \times 10^{-6}$) significantly improved at discriminating
469 the three subject groups when compared to individual markers. An LDA plot using the feature set comprised
470 of a combination of six miRNA markers shows a small overlap across nPCa, mPCa, and BPH patients (Fig.
471 7g). As shown in Fig. 7h, the PCa signature was able to discriminate PCa from BPH with a sensitivity,
472 specificity and accuracy of 100% in the validation cohort. In addition, only two mPCa and one nPCa case
473 were misclassified, leading to an overall accuracy of 90.6% (95% CI, 75.0 to 98.0%; Supplementary Fig.
474 S11b). Collectively, these comparative results further showed that our SORTER approach had potential
475 adaptability for molecular phenotyping and improved diagnostic performance for early-stage cancer.

476 ## Discussion

477 Exosomes carry a specific subset of molecular payloads (e.g., RNA, DNA, protein, and lipids) inherited
478 from the parent cells and function as essential mediators in short- and long-distance intercellular
479 communication.[50, 51] Accumulated evidence has recently shown that the abnormal expression of miRNAs in
480 tumor-associated exosomes is highly associated with cancer development, invasion, and metastasis.[52, 53]
481 Therefore, miRNAs in tumor-associated exosomes are gaining popularity as a source of non-invasive
482 biomarkers in interrogating the biology and heterogeneity of malignancies, as well as improving cancer
483 diagnosis and prognosis. However, current technologies for assessing miRNA profiles in tumor-derived
484 exosomes remain challenging due to the clinical background interference[54, 55], highly heterogeneous EV

485 subtypes [56, 57], and wide concentration range of different exosomal miRNA[23, 24]. To address these issues, we
486 developed a highly versatile and powerful SORTER technique that enables rapid and precise recognition and
487 simultaneous miRNA profiling of tumor-derived exosomes directly from clinical plasma samples.

488 Regarding subpopulation differentiation, the conventional techniques for tumor-derived exosome
489 identification/isolation are primarily univariate (e.g., single-target recognition)[14, 33, 58], which are achieved
490 by using antibodies, peptides, and aptamers to bind surface protein receptors. However, these techniques
491 may be interfered with by the coexisting components (e.g., microvesicles, apoptotic bodies, normal-derived
492 exosomes, and free molecules) with overlapping features in their composition and thus lack tumor
493 specificity.[32, 59, 60] In this study, we first presented a combinatorial SORTER methodology that incorporates
494 dual-surface-protein synergistic recognition to precisely label tumor-derived exosomes in unextracted
495 plasma samples. Specifically, our approach utilized two allosteric aptamers of exosomal marker CD63 and
496 tumor marker EpCAM to create a unique orthogonal identity barcode on the tumor-derived exosome surface,
497 permitting targeted recognition and controlled fusion of complementary DNA-anchored liposome probes.
498 We first evaluated the recognition specificity of SORTER for tumor LNCaP Exo and normal BPH-1 Exo by
499 flow cytometry and TIRFM measurements (Fig. 2a-c). Our results showed that the CD63 and EpCAM
500 proteins are overexpressed and coexisted on a single tumor exosome surface, indicating that the synergistic
501 recognition of CD63 and EpCAM proteins is a feasible choice for tracing tumor-derived exosomes. We then
502 demonstrated the formed orthogonal barcode-anchored on the tumor-derived exosome surface and the high
503 reliability of the hybridization of DNA Tags and orthogonal barcode-anchored exosomes by flow cytometry
504 and TIRFM results (Fig. 2d-f). Next, we demonstrated the significant dual-surface-protein-mediated
505 orthogonal fusion events by FRET, TIRFM, TEM, and DLS (Fig. 3b-g) measurements. Distinct from the
506 conventional identification/isolation techniques, we utilized the selectivity of SORTER to minimize the
507 interference of non-specific vesicles and free molecules that enable recognize of tumor-derived exosomes in
508 plasma samples rapidly and precisely, avoiding lengthy pre-isolation/purification procedures and minimizing
509 the non-specific interference of contaminated vesicles.

510 For quantitative analysis of exosomal miRNAs, most of the existing techniques (i.e., qRT-PCR, NGS)
511 measure the total miRNA concentration in the biofluids or the ensemble of EV populations, which are prone
512 to the interference of non-specific vesicles and free miRNAs[15, 16, 42], rendering the conclusions drawn less

predictive in complex clinical scenarios. Moreover, femtomolar sensitivity is essential for in situ miRNA profiling of exosomes, where the concentrations of miRNAs are deficient (roughly 1 copy/10^6 EVs to 1 copy/1 EV)[22-24]. In this study, the SORTER incorporates multiple parallel processes, including exosome recognition, importing probes, miRNA signal transduction, and amplification, allowing for a fast, sensitive, and multiparametric profiling of miRNAs in tumor-derived exosomes directly from clinical plasma samples. We first evaluated the testing capabilities of SORTER for tumor LNCaP- and normal BPH-1 exosomal miR-21 using FL, flow cytometry, and TIRFM measurements (Fig. 4b-e). These results showed an elevated amount of miR-21 in the tumor LNCaP Exo and the sensitivity of SORTER for quantification of miR-21 as low as femtomolar. Next, we evaluated the performance of SORTER by measuring the expression levels of six miRNAs in different cells exosomes and clinical plasma samples (Fig. 4f and 4g). Compared to previously reported techniques, the SORTER affords three significant advantages as follows: First, the SORTER does not involve any exosome lysis and RNA preparation procedures, which markedly simplifies the experimental operation, reduces the processing time, bypasses the dilution of low-abundance miRNAs, and prevents sample loss during exosome lysing and RNA extraction procedures. Second, the technique incorporates dual-surface-protein synergistic recognition to sort and analyze tumor-derived exosomes precisely, a small yet significant subpopulation of extracellular vesicles, improving the diagnostic and prognostic accuracy of exosomal miRNA-based liquid biopsy. Third, this technique requires only small-volume plasma samples (~0.2 μL), a short assay time of ~2 h by skipping lengthy pre-isolation/purification processes, and is high throughput compatible with 96/384 well plate, opening a new way for non-invasive and high-accuracy cancer screening and progress monitoring.

Concerning exosomal miRNA profiling for liquid biopsy applications, the SORTER enables the capture of the information of tumor-derived exosome ($CD63^+EpCAM^+$ EVs) subpopulation in complex clinical scenarios, which is often missed in other approaches and only accessible via single-exosome miRNA analysis. Although we cannot spatially determine the fusion proportion of each liposome probe to an individual tumor-derived exosome, statistically, the multiparametric miRNA profiling by SORTER still reflects the compositional nature of the studied tumor-derived exosomes. Here, we made a comparative study of single- and dual-surface-protein-mediated orthogonal fusion (SORTER) to direct subpopulation differentiation and miRNA profiling directly from plasma samples in a clinical cohort involving 20 PCa patients and 10 BPH

controls. We first investigated the relationship between clusters of exosome subpopulations by unsupervised hierarchical clustering analysis to corroborate the validity of the analytical data obtained by SORTER (Fig. 5d). Then, the Pearson correlation of individual markers showed weak correlations in these EV subpopulations (Fig. 5e-g). Next, we harnessed LDA methods to compile all miRNA profiles to improve the diagnostic performance of exosome-based liquid biopsy in differentiating PCa and BPH groups (Fig. 5h-o). Our data showed the PCa signature in $CD63^{+}EpCAM^{+}$ EVs shows an extremely high sensitivity of 100%, specificity of 100%, and accuracy of 100% for distinguishing between PCa from BPH compared with $CD63^{+}$ EVs [with 50.0 sensitivity, 90.0% specificity, and 76.7% accuracy] and $EpCAM^{+}$ EVs [with 90.0% sensitivity, 100% specificity, and 96.7% accuracy]. These results demonstrated that our SORTER could recognize and analyze tumor-derived exosomes precisely, thus improving the diagnostic performance of exosome-based liquid biopsy. We also evaluate the diagnostic adaptability of SORTER for PCa diagnosis and stratification in a clinical cohort (n = 74, Fig. 6 and Fig. 7). In comparison to the serum PSA marker [training cohort with 0.722 AUC; validation cohort with 0.867 AUC] or single-EV marker analyses [training cohort with 0.901-0.984 AUC; validation cohort with 0.802-0.990 AUC], our results showed that the PCa signature [training cohort with 1.00 AUC; validation cohort with 1.00 AUC] provided excellent diagnostic performance in differentiating PCa patients and BPH controls. Combining six miRNA markers tested (PCa signature), the SORTER was able to discriminate PCa from BPH with a sensitivity, specificity, and accuracy of 100% in the training and validation cohorts. Additionally, the PCa signature exhibits high overall accuracy in distinguishing BPH controls and two subgroups of nPCa and mPCa patients, with 100% in a training cohort and 90.6% in an independent validation cohort. These comparative results showed that our SORTER approach had potential adaptability for molecular phenotyping and improved diagnostic performance for cancer.

The technology of SORTER exhibited the unique advantages of being rapid, non-invasive, avoiding separation, scalability, and high accuracy in assessing miRNA profiles of tumor-derived exosomes. The SORTER is capable of high-throughput analysis in clinical studies, and the accuracy has been improved by integrating machine learning into data processing. With its robust ability to differentiate tumor-derived exosomes in clinical plasma samples, the SORTER could be readily expanded to measure, beyond miRNAs, other diverse molecules (e.g., internal proteins, lipids, and metabolites). The barcoding capacity of this

technology can be readily enhanced by designing new allosteric-aptamer probes, allowing for measuring other EVs of molecular subtypes (e.g., different cell origins). The SORTER will contribute to the advancement of the liquid biopsy field and be a clinically feasible tool for disease screening, classification, and progress monitoring in complex clinical settings.

Methods

Cells and culture conditions

The human prostate cancer cell lines LNCaP, DU145, and PC-3 were purchased from the China Center for Type Culture Collection (Shanghai, China). The human prostatic hyperplasia cell line BPH-1 was bought from the Yaji Biotechnology Co., Ltd (Shanghai, China). DU145 cell was maintained in an exosome-depleted DMEM medium. LNCaP, PC-3, and BPH-1 cells were maintained in an exosome-depleted RPMI1640 medium. All cell line media were supplemented with 10% vesicle-depleted fetal bovine serum (FBS) and 1% penicillin-streptomycin in a humidified incubator with constant temperature (37 °C) and 5% CO_2. Vesicle-depleted FBS was prepared by centrifuging FBS for 10 h at 100,000 g, then passing the supernatant through a 0.22 μm filter.

Exosome isolation by standard differential ultracentrifugation.

The cell culture media were collected for cell-derived exosome isolation until cells reached 80-90% confluency. The medium was packaged into six ultracentrifuge tubes with a weight difference between every pair of tubes smaller than 0.02 g. First, the collected media were centrifuged at 3000×g for 20 min at 4 °C to remove cells and large debris. Then, the resulting supernatant was centrifuged at 16,500×g for 45 min at 4 °C to pellet microvesicles. After that, the supernatant was ultracentrifuged at 100,000g for 2 h to collect exosomes. The resulting pellets were resuspended and washed with filtered PBS, followed by another centrifugation of 100,000 g for 2 h at 4 °C. Finally, the resulting exosomes were resuspended in filtered PBS and stored at -80 °C for further use.

Clinical samples.

Clinical samples of patients with prostate cancer and benign prostatic hyperplasia were obtained from Renji Hospital of Shanghai Jiaotong University School of Medicine. All relevant ethical regulations were complied with. All samples (n =74) were anonymized, and only the age of PSA and pathological diagnosis were recorded. In the clinical cohorts, the prostate cancer patients (n=47) had been diagnosed, and the benign prostatic hyperplasia controls (n=27) had no history of cancer before sample collection. Relevant information on the human participants in the clinical was presented in Supplementary Table S2.

Before use, the blood samples were centrifuged at 3,000 g for 10 min to obtain cell-free plasma. Then, the human plasma was centrifuged at 4 °C at 10,000g for 20 min to remove large vesicles. The plasma samples were filtered with a 0.45 μm filter into a new EP tube and stored at -80 °C for further use.

Synthesis and characterization of Au nanoflares

Au nanoflares (Au NFs) were obtained in the following manner. Before use, citrate-capped gold nanoparticles (Au NPs, 13 nm ± 2 nm) were prepared according to a literature-reported method[61]. Then, 5'-SH and 3'-FAM-labeled DNA probes (25 μL, 10 μM) were mixed with 100 μL Au NPs solution. The mixture was then placed in a -80 °C freezer for 2 h, followed by thawing at room temperature. Following that, the resultant FAM-DNA-labeled Au NPs solution was centrifuged (13000 rpm, 8 min) to remove the free DNA before being dissolved in PBS buffer (10 mM, pH 7.4) with 5 mM $MgCl_2$. Next, 10 μL BSA (5%) was added to the FAM-DNA-labeled Au NPs solution, which was then shaken at RT for 1 h. Finally, the resultant Au NFs solution was centrifuged (13000 rpm, 8 min) to remove the free molecules and dissolved in Tris-HCl buffer (10 mM, pH 7.4) containing 10 mM $MgCl_2$ for further use. The concentration of Au NFs was determined as 15 nM based on the molar extinction coefficient of 2.7×10^{8} M^{-1} cm^{-1} at 520 nm. The loading density of DNA probes on each Au NFs was determined as 75 nM based on the molar extinction coefficient of 2.33×10^{5} $M^{-1}cm^{-1}$ at 260 nm.

Synthesis and characterization of liposome probes.

Before use, the liposome solution (25 mg mL^{-1}) from 1,2-Dioleoyl-sn-glycero-3-phosphocholine/1,2-

dioleoyl-sn-glycero-3-phosphoethanolamine/Cholesterol (DOPC/DOPE/Chol; 2:1:1, molar ratio) was obtained according to a literature-reported method.[62] Then, 300 μL reaction mixture containing 1 mg mL^{-1} liposome, 0.2×DSN buffer, 1 U DSN, 20 U RNase inhibitor, and 15 nM Au NFs was co-extruded repeatedly 20 times through 200 nm polycarbonate porous membranes (Whatman NucleoporeTrack-Etched Membranes) using a mini-extruder (Avanti Polar Lipids). Next, 15 μL Chol-labeled DNA tags (Tags, 10 μM) were incubated with the above liposome solution at RT for 1 h. Finally, the resultant liposome probes (Tags-Lipo@Au NFs) were purified by ultrafiltration to remove the free products and dissolved in Tris-HCl buffer (10 mM, pH 7.4) containing 10 mM $MgCl_2$ for further use.

Dual-surface-protein labeling on tumor-derived exosomes.

For flow cytometry analysis of nine protein expressions of the exosome, we utilized the latex aldehyde beads (Thermo Fisher Scientific, 3 μm) to immobilize human prostate cancer LNCaP and PC-3 cell-, as well as prostatic hyperplasia BPH-1 cell-derived exosomes. First, 20 μg of LNCAP or PC-3, BPH-1 cell-derived exosomes were incubated with 8 μL of latex aldehyde beads for 15 min, followed by adding 1 mL of filtered PBS for another 3 h. Then, the reaction was stopped by adding 20 μL of 1 M glycine and 80 μL of 20 % BSA (w/v) for 30 min. After that, the exosome-coated beads were washed twice by centrifugation (3 min, 6,000 rpm) and then resuspended in 60 μL filtered PBS (containing 0.5% BSA). Next, 5 μL of exosome-coated beads were incubated with 0.25 μM FAM-labeled aptamer probes in 100 μL binding buffer (PBS with 0.5 mM $MgCl_2$, pH 7.4) for 2 h at 4 °C. After washing 2 times, the fluorescence intensity of exosome-coated beads was detected by flow cytometry.

For flow cytometry or TIRFM analysis of CD63-S-L and EpCAM-S-L-mediated orthogonal labeling on a single exosome surface, 5 μL of LNCAP Exo-coated beads (the preparation process was as described above) or 10 μL of 1.14 μg μL^{-1} LNCAP Exo were incubated with 0.25 μM Cy5-labeled EpCAM-S-L and FAM-labeled CD63-S-L probes in 100 μL binding buffer (PBS with 0.5 mM $MgCl_2$, pH 7.4) for 2 h at 4 °C. After washing 2 times, the fluorescence intensity of exosome-coated beads was analyzed by flow cytometry or TIRFM. BPH-1 Exo was used as a negative control.

Zipperlike hybridization of the orthogonal barcode-anchored exosome and complementary DNA tags.

For flow cytometry or TIRFM analysis of zipperlike hybridization on the tumor-derived exosome surface, 5 μL of LNCAP/BPH-1 Exo-coated beads (the preparation process was as described above) or 10 μL of 1.14 μg μL^{-1} LNCAP Exo were incubated with 5 μL of 5 μM Cy5-labeled EpCAM-S-L and FAM-labeled DNA tags (FAM-Tags), and 5 μL of 5 μM non-fluorescent CD63-S-L probes in 100 μL binding buffer (PBS with 0.5 mM $MgCl_2$, pH 7.4) for 2 h at 4 °C. After washing 2 times, the fluorescence intensity of exosome-coated beads was detected by flow cytometry or TIRFM. The hairpin rCD63 probe (rCD63-S-L, only the aptamer domain was replaced by a random sequence) was used as a negative control.

Dual-surface-protein-guided liposome probe fusion studies.

For the lipid-mixing FRET decrease assay, the dynamic process of orthogonal barcode-anchored LNCAP Exo (Orth-Exo) and Tags-Liposome (Tags-Lipo) membrane fusion was investigated using a standard FRET decrease assay. First, 100 μL of 1.0×10^{10} particles mL^{-1} Lipo were incubated with 20 μM DiO and 20 μM DiI for 30 min at 37 °C. After that, the DiI and DiO double-labeled Lipo (Lipo-DiI-DiO) were incubated with 5 μL of 5 μM Tags for 1 h at RT, obtaining the DiI and DiO double-labeled Tags-Lipo (Tags-Lipo-DiI-DiO) products. The free products were removed by ultrafiltration at 13000 g for 20 min 3 times at each step. Finally, 100 μL of 1× or 10×10^{10} particles mL^{-1} Exo, 5 μL of 5 μM CD63-S-L, 5 μL of 5 μM EpCAM-S-L were incubated with 100 μL Tags-Lipo-DiI-DiO for 2 h at 37 °C, and then the mixture was measured using fluorescence spectrometer or using fluorescence kinetic analysis. The stochastic fusion between Exo and Lipo-DiI-DiO was used as a negative control.

For TIRFM studies, 100 μL of 1.0×10^{10} particles mL^{-1} LNCAP Exo was incubated with 20 μM DiO for 30 min at 37 °C. After that, the prepared DiO-labeled Orth-Exo products were dissolved in 100 μL PBS buffer (10 mM, pH 7.4) containing 5 mM $MgCl_2$. Meantime, 100 μL of 1.0×10^{10} particles mL^{-1} Lipo was labeled by DiI using the same method and then incubated with 5 μL of 10 μM Tags for 1 h at RT, obtaining the Tags-Lipo-DiI products. The free products were removed by ultrafiltration at 13000 g for 20 min 3 times at each step. Finally, 100 μL DiO-labeled Orth-Exo, 5 μL of 5 μM CD63-S-L, and 5 μL of 5 μM EpCAM-S-L were incubated with 100 μL DiI-labeled Tags-Lipo for 2 h at 37 °C, and the mixture was imaged using

the TIRFM. The stochastic fusion of Exo-DiO and Lipo-DiI was used as negative control.

For DLS studies, 100 μL of 1.0×10^{10} particles mL^{-1} Lipo was incubated with 5 μL of 5 μM Tags for 1 h at RT. Then, the free products were removed by ultrafiltration at 13000 g for 20 min 3 times. After that, the prepared Tags-Lipo products were dissolved in 100 μL PBS buffer (10 mM, pH 7.4) containing 5 mM $MgCl_2$. Finally, 100 μL of 1.0×10^{10} particles mL^{-1} LNCAP Exo, 5 μL of 5 μM CD63-S-L, and 5 μL of 5 μM EpCAM-S-L were incubated with 100 μL Tags-Lipo products, and the mixture was measured at 37 °C under different time intervals. The group of Exo and Lipo was used as negative controls.

For TEM imaging, the fusion mixtures of Tags-Lipo@Au NFs and Orth-Exo (the preparation process was as described above) were added onto a 150 mesh formvar copper grid or ITO glass and incubated for 10 min. After washing with ultrapure water, the samples were treated with 2.5% glutaraldehyde in PBS for 30 min, then rinsed for 15 min to fix the particles. Next, the samples were negatively stained with 2% uranyl acetate for 10 min and rinsed for 10 min with water. Samples were dried and visualized using TEM imaging. Orth-Exo and Tags-Lipo@Au NFs were used as negative controls.

Profiling of tumor-derived exosomal miRNA.

To clarify the SORTER approach for tumor-derived exosomal miRNA analysis, the LNCAP Exo solution was prepared by serial dilutions of the stock solution in 1 mL PBS or 100 folds-diluted EV-depleted plasma. Specifically, 5 μL of 1 μM CD63-S-L, 5 μL of 1 μM EpCAM-S-L, and liposome probes (20 μL, 1.0×10^{10} particles mL^{-1}) were incubated with 20 μL of the prepared exosome solution for 2 h at 37 °C. Finally, the mixture was measured using a multi-detection microplate reader. The group of exosomes and liposomes was used as negative controls.

To achieve the tumor-derived exosomal miRNA analysis in clinical plasma samples directly, 5 μL of 1 μM CD63-S-L, 5 μL of 1 μM EpCAM-S-L, and liposome probes (20 μL, 1.0×10^{10} particles mL^{-1}) were incubated with 20 μL of 100-fold dilution plasma samples for 2 h at 37 °C. Finally, the mixture was measured using a multi-detection microplate reader. The group of exosomes and liposomes was used as negative controls.

693 **Statistical analyses.**

694 Mean, SD, and LOD were calculated with standard formulas. Significance tests were obtained via a
695 two-tailed Student's *t*-test. The intensities of individual miRNA markers detected by the SORTER approach
696 used Min-max normalization. The PCa signature was calculated as the weighted sum of the normalized
697 intensities of six miRNA markers by LDA, respectively. For binary classification, *P* values for pairwise
698 comparisons were performed using a nonparametric, two-tailed Mann-Whitney *U* test. For ternary
699 classification, the overall and group pair *P* values were determined using Kruskal-Wallis one-way ANOVA
700 with post hoc Dunn's test for pairwise multiple comparisons. Hierarchical clustering was performed for the
701 analysis markers using the "pheatmap" package in the R language. ROC analyses were constructed for
702 individual markers or marker combinations to evaluate the AUC, sensitivity and specificity, and accuracy of
703 a cancer diagnosis. The training cohort (n = 42) was first analyzed to generate the discriminant function
704 model, which was used to classify the patients in the validation cohort (n = 32). The optimal cutoff points
705 were selected using Youden's index based on the training cohort, which was applied to evaluate the validation
706 cohort's sensitivity, specificity, and accuracy. The t-distributed stochastic neighbor embedding (t-SNE) was
707 performed using six markers as the input for binary classification (PCa and BPH). All statistical analyses
708 were performed at 95% ($P < 0.05$) CIs using OriginPro 2018, GraphPad Prism (v.8.0), and R software
709 (version 4.1.2).

710 **Data availability**

711 The source data underlying Fig. 3b, c, d, e, 4b, e, f, g, Fig. 5, Fig. 6, and Fig. 7 were provided as a Source
712 Data file. All other data are available from the authors upon reasonable request.

713 ## References

714 1. Mahtal, N., Lenoir, O., Tinel, C., Anglicheau, D. & Tharaux, P.L. MicroRNAs in kidney injury and disease.
715 *Nat. Rev. Nephrol.* **18**, 643-662 (2022).
716 2. Clyde, D. Target-directed microRNA degradation in Drosophila. *Nat. Rev. Genet.* **23**, 713 (2022).
717 3. Jafari, N., Llevenes, P. & Denis, G.V. Exosomes as novel biomarkers in metabolic disease and obesity-
718 related cancers. *Nat. Rev. Endocrinol.* **18**, 327-328 (2022).
719 4. Lempriere, S. Exosomal microRNA is promising biomarker in PD. *Nat. Rev. Neurol.* **18**, 65 (2022).

5. van Eijndhoven, M.A.J., Baglio, S.R. & Pegtel, D.M. Packaging RNA drugs into extracellular vesicles. *Nat. Biomed. Eng.* **4**, 6-8 (2020).
6. Ji, C. & Guo, X. The clinical potential of circulating microRNAs in obesity. *Nat. Rev. Endocrinol.* **15**, 731-743 (2019).
7. Hu, T., Wolfram, J. & Srivastava, S. Extracellular Vesicles in Cancer Detection: Hopes and Hypes. *Trends Cancer* **7**, 122-133 (2021).
8. Kalluri, R. & LeBleu, V.S. The biology, function, and biomedical applications of exosomes. *Science* **367**, 640 (2020).
9. Isaac, R., Reis, F.C.G., Ying, W. & Olefsky, J.M. Exosomes as mediators of intercellular crosstalk in metabolism. *Cell Metab.* **33**, 1744-1762 (2021).
10. Clancy, J.W. & D'Souza-Schorey, C. Tumor-Derived Extracellular Vesicles: Multifunctional Entities in the Tumor Microenvironment. *Annu. Rev. Pathol. Mech. Dis.* **18**, 205–229 (2023).
11. Li, C. et al. Roles and mechanisms of exosomal non-coding RNAs in human health and diseases. *Signal Transduct. Target Ther.* **6**, 383 (2021).
12. Sun, N. et al. Purification of HCC-specific extracellular vesicles on nanosubstrates for early HCC detection by digital scoring. *Nat. Commun.* **11**, 4489 (2020).
13. Liu, C. et al. Low-cost thermophoretic profiling of extracellular-vesicle surface proteins for the early detection and classification of cancers. *Nat. Biomed. Eng.* **3**, 183-193 (2019).
14. Liang, K. et al. Nanoplasmonic Quantification of Tumor-derived Extracellular Vesicles in Plasma Microsamples for Diagnosis and Treatment Monitoring. *Nat. Biomed. Eng.* **1**, 0021 (2017).
15. Bordanaba-Florit, G., Royo, F., Kruglik, S.G. & Falcon-Perez, J.M. Using single-vesicle technologies to unravel the heterogeneity of extracellular vesicles. *Nat. Protoc.* **16**, 3163-3185 (2021).
16. Willms, E., Cabañas, C., Mäger, I., Wood, M.J.A. & Vader, P. Extracellular Vesicle Heterogeneity: Subpopulations, Isolation Techniques, and Diverse Functions in Cancer Progression. *Front. Immunol.* **9**, 738 (2018).
17. O'Brien, K., Breyne, K., Ughetto, S., Laurent, L.C. & Breakefield, X.O. RNA delivery by extracellular vesicles in mammalian cells and its applications. *Nat. Rev. Mol. Cell Biol.* **21**, 585-606 (2020).
18. Hu, J. et al. A signal-amplifiable biochip quantifies extracellular vesicle-associated RNAs for early cancer detection. *Nat. Commun.* **8**, 1683 (2017).
19. Srinivasan, S. et al. Small RNA Sequencing across Diverse Biofluids Identifies Optimal Methods for exRNA Isolation. *Cell* **177**, 446-462 (2019).
20. Garcia-Martin, R. et al. MicroRNA sequence codes for small extracellular vesicle release and cellular retention. *Nature* **601**, 446-451 (2022).
21. Guay, C. et al. Lymphocyte-Derived Exosomal MicroRNAs Promote Pancreatic beta Cell Death and May Contribute to Type 1 Diabetes Development. *Cell Metab.* **29**, 348-361 (2019).
22. Chevillet, J.R. et al. Quantitative and stoichiometric analysis of the microRNA content of exosomes. *Proc. Natl. Acad. Sci. U.S.A.* **111**, 14888-14893 (2014).
23. Vickers, K.C., Palmisano, B.T., Shoucri, B.M., Shamburek, R.D. & Remaley, A.T. MicroRNAs are transported in plasma and delivered to recipient cells by high-density lipoproteins. *Nat. Cell Biol.* **13**, 423-433 (2011).
24. Mori, M.A., Ludwig, R.G., Garcia-Martin, R., Brandao, B.B. & Kahn, C.R. Extracellular miRNAs: From Biomarkers to Mediators of Physiology and Disease. *Cell Metab.* **30**, 656-673 (2019).
25. Chen, X. et al. High-Fidelity Determination and Tracing of Small Extracellular Vesicle Cargoes. *Small* **16**,

2002800 (2020).
26. Zhou, J. et al. High-throughput single-EV liquid biopsy: Rapid, simultaneous, and multiplexed detection of nucleic acids, proteins, and their combinations. *Sci. Adv.* **6** eabc1204 (2020).
27. Cao, Y. et al. Molecular Characterization of Exosomes for Subtype-Based Diagnosis of Breast Cancer. *J. Am. Chem. Soc.* **144**, 13475-13486 (2022).
28. Gao, X. et al. Rapid Detection of Exosomal MicroRNAs Using Virus-Mimicking Fusogenic Vesicles. *Angew. Chem. Int. Ed.* **58**, 8719-8723 (2019).
29. Zhao, J. et al. Thermophoretic Detection of Exosomal microRNAs by Nanoflares. *J. Am. Chem. Soc.* **142**, 4996-5001 (2020).
30. Zhang, P. et al. Ultrasensitive detection of circulating exosomes with a 3D-nanopatterned microfluidic chip. *Nat. Biomed. Eng.* **3**, 438-451 (2019).
31. Deng, J. et al. Rapid One-Step Detection of Viral Particles Using an Aptamer-Based Thermophoretic Assay. *J. Am. Chem. Soc.* **143**, 7261-7266 (2021).
32. Cocozza, F., Grisard, E., Martin-Jaular, L., Mathieu, M. & Thery, C. SnapShot: Extracellular Vesicles. *Cell* **182**, 262-262 (2020).
33. Tian, F. et al. Protein analysis of extracellular vesicles to monitor and predict therapeutic response in metastatic breast cancer. *Nat. Commun.* **12**, 2536 (2021).
34. Deng, J. et al. One-Step Thermophoretic AND Gate Operation on Extracellular Vesicles Improves Diagnosis of Prostate Cancer. *Angew. Chem. Int. Ed.* **134**, e202207037 (2022).
35. Li, Y. et al. Molecular Identification of Tumor-Derived Extracellular Vesicles Using Thermophoresis-Mediated DNA Computation. *J. Am. Chem. Soc.* **143**, 1290-1295 (2021).
36. Yang, Y. et al. Aptamer-Based Logic Computing Reaction on Living Cells to Enable Non-Antibody Immune Checkpoint Blockade Therapy. *J. Am. Chem. Soc.* **143**, 8391-8401 (2021).
37. Chang, X. et al. Construction of a Multiple-Aptamer-Based DNA Logic Device on Live Cell Membranes via Associative Toehold Activation for Accurate Cancer Cell Identification. *J. Am. Chem. Soc.* **141**, 12738-12743 (2019).
38. Lin, B.Q. et al. Tracing Tumor-Derived Exosomal PD-L1 by Dual-Aptamer Activated Proximity-Induced Droplet Digital PCR. *Angew. Chem. Int. Ed.* **60**, 7582-7586 (2021).
39. Zhang, J. et al. Spatially Patterned Neutralizing Icosahedral DNA Nanocage for Efficient SARS-CoV-2 Blocking. *J. Am. Chem. Soc.* **144**, 13146-13153 (2022).
40. Wu, L. et al. Aptamer-Based Detection of Circulating Targets for Precision Medicine. *Chem. Rev.* **121**, 12035-12105 (2021).
41. Xie, S. et al. Engineering Aptamers with Selectively Enhanced Biostability in the Tumor Microenvironment. *Angew. Chem. Int. Ed.* **61**, e202201220 (2022).
42. Verweij, F.J. et al. The power of imaging to understand extracellular vesicle biology in vivo. *Nat. Methods* **18**, 1013-1026 (2021).
43. Siegel, R.L., Miller, K.D., Fuchs, H.E. & Jemal, A. Cancer Statistics, 2021. *CA: Cancer J. Clin.* **71**, 7-33 (2021).
44. Manak, M.S. et al. Live-cell phenotypic-biomarker microfluidic assay for the risk stratification of cancer patients via machine learning. *Nat. Biomed. Eng.* **2**, 761-772 (2018).
45. Jaratlerdsiri, W. et al. African-specific molecular taxonomy of prostate cancer. *Nature* **609**, 552-559 (2022).
46. Ankerst, D.P. & Thompson, I.M. Sensitivity and specificity of prostate-specific antigen for prostate cancer

detection with high rates of biopsy verification. *Arch. Ital. Urol. Androl.* **78**, 125-129 (2006).
47. Welch, H.G., Schwartz, L.M. & Woloshin, S. Prostate-specific antigen levels in the United States: implications of various definitions for abnormal. *J. Natl. Cancer Inst.* **97**, 1132-1137 (2005).
48. Eminaga, O. et al. The expression profiles of miRNAs in the progression of prostate cancer from high-grade prostatic intraepithelial neoplasia to metastatic diseases. *J. Clin. Oncol.* **34** (2016).
49. Zaporozhchenko, I.A. et al. Urine cell-free and extracellular vesicle cargo miRNAs as biomarkers for prostate cancer diagnosis. *Ann. Oncol.* **30** (2019).
50. Reategui, E. et al. Engineered nanointerfaces for microfluidic isolation and molecular profiling of tumor-specific extracellular vesicles. *Nat. Commun.* **9**, 175 (2018).
51. Exosome Profiling Pinpoints Cancer Type. *Cancer Discov.* **10**, 1619 (2020).
52. Godlewski, J. et al. MicroRNA Signatures and Molecular Subtypes of Glioblastoma: The Role of Extracellular Transfer. *Stem. Cell Rep.* **8**, 1497-1505 (2017).
53. Zhu, L. et al. Exosomal tRNA-derived small RNA as a promising biomarker for cancer diagnosis. *Mol. Cancer* **18**, 74 (2019).
54. Zhang, C. et al. Cancer diagnosis with DNA molecular computation. *Nat. Nanotechnol.* **15**, 709-715 (2020).
55. Wang, Z.X. et al. High-throughput intracellular biopsy of microRNAs for dissecting the temporal dynamics of cellular heterogeneity. *Sci. Adv.* **6**, eaba4971 (2020).
56. Marar, C., Starich, B. & Wirtz, D. Extracellular vesicles in immunomodulation and tumor progression. *Nat. Immunol.* **22**, 560-570 (2021).
57. Grange, C. & Bussolati, B. Extracellular vesicles in kidney disease. *Nat. Rev. Nephrol.* **18**, 499-513 (2022).
58. Lin, B. et al. Tracing Tumor-Derived Exosomal PD-L1 by Dual-Aptamer Activated Proximity-Induced Droplet Digital PCR. *Angew. Chem. Int. Ed.* **60**, 7582-7586 (2021).
59. Chen, Y. et al. Exosome detection via the ultrafast-isolation system: EXODUS. *Nat. Methods* **18**, 212-218 (2021).
60. Zhang, H. et al. Identification of distinct nanoparticles and subsets of extracellular vesicles by asymmetric flow field-flow fractionation. *Nat. Cell Biol.* **20**, 332-343 (2018).
61. Liu, J. & Lu, Y. Preparation of aptamer-linked gold nanoparticle purple aggregates for colorimetric sensing of analytes. *Nat. Protoc.* **1**, 246-252 (2006).
62. Loffler, P.M.G. et al. A DNA-Programmed Liposome Fusion Cascade. *Angew. Chem. Int. Ed.* **56**, 13228-13231 (2017).

Acknowledgements

This work was supported by the National Key R&D Program of China (2022YFA1305200, 2019YFA0905800), the National Natural Science Foundation of China (22004084, 21927806, 21735004, 82072847, and 22022408), the Program for Changjiang Scholars and Innovative Research Team in University (Grant IRT13036), and Innovative Research Team of High-level Local Universities in Shanghai (SHSMU-ZLCX20212601).

Author contributions

Y.L. and P.Z. conceived the project. Y.L. and X.F performed the experiments. X.F, Y.D. and G.Z. prepared the exosomes. X.F. and W.X. provided clinical samples. Y.L., X.F and J.S analyzed the data and interpreted the results. Y.Z., W.X., P.Z., and C.Y. supervised the project. Y.L., P.Z. and C.Y. wrote the manuscript. All authors joined in the critical discussion and edited the paper.

Competing interests

The authors declare no competing interests.

Supplementary Files

This is a list of supplementary files associated with this preprint. Click to download.

- SupplementaryInformation.pdf